Forces Due to Detonation Propagation in a Bend

J. E. Shepherd and R. Akbar
Graduate Aeronautical Laboratories
California Institute of Technology
Pasadena, CA 91125

Explosion Dynamics Laboratory Report FM2008.002

February 24, 2009
Revision of 19 May, 2010

Prime Sponsor: US Department of Energy, Office of River Protection, Hanford, WA.
Sponsor: Project Assistance Corporation, contract ORP-CAL001.

Abstract

The purpose of this study is to develop simple analytical models for the forces created on a piping system due to an internal detonation wave propagating through a bend. These models are designed to be used as inputs to vibration studies that are carried out with finite-element models of piping and support systems. For simulation tools like ME101 that consider piping systems as structural frames, a point force model is developed that can be applied as a specified external load at the location of the bend. For simulation tools like ANSYS that model piping systems as an elastic material with a subdivision into elements in both axial and circumferential directions, an internal pressure loading model is developed to enable the specification of a traveling load inside the bend that simulates both the mean internal pressure and asymmetry created by flow through the bend.

Contents

List of Figures

List of Tables

1 Introduction

This report develops and analyzes two simple analytical models of forces created by detonation waves propagating in a bend. The predictions of these models are compared to data obtained in experiments specifically carried out to measure strains and forces in a model piping system. Those experiments are described briefly in this document and in more detail within a subsequent report, Shepherd and Akbar (2010). This study is just one component of a larger, multi-organization project on the engineering evaluation of the safety basis for the Waste Treatment Plant under construction at Hanford, WA.

The plan of the report is as follows: First, we give a brief introduction to the key issues associated with the quantitative analysis of piping systems for internal explosions. Second, we discuss typical piping vibrational frequencies for straight sections and sections with bends. Results of experiments on detonation waves in bends is given. Third, the control volume approach to analyzing and modeling forces in piping components is formulated and applied to a bend. Fourth, the ideal detonation wave model is used to estimate momentum flux for the control volume approach and results in a simple estimate for bend forces based on a quasi-steady approximation to flow in the bend. Fifth, a model pressure wave profile is developed that matches the control volume result for the force and has an average internal pressure that matches the average hoop strain. Sixth and finally, the results of the models are compared with experiments carried out in a piping specimen with a single 90-degree bend in 2-in schedule 40 stainless steel pipe.

The key issue (Shepherd, 2009) in the quantitative analysis of potential explosion hazards in piping systems is the estimation of the magnitude of the stresses and displacements during and after the explosion event. There are several types of events, which can be categorized as: a) low-speed deflagration (flame), b) high-speed deflagration, c) accelerating deflagration followed by transition to detonation (DDT), and d) rapid onset of a detonation that propagates through a large portion of the piping system. Each type of event has to be considered separately in a hazard analysis with consideration of both mechanical and thermal effects on the piping and support systems. Slow events (a in the list above) can be treated quasi-statically with the usual methods of pressure vessel analysis but with particular attention to the thermal stresses. Rapid events (b-d in the list above) must be treated using methods of dynamics since they will excite vibrations in the piping system and supports. The division into slow and fast events depends on the time scale of the explosion relative to the structural response times.

The vibrations are principally of two types: I) localized vibrations that are excited by shock or detonation waves and II) vibrations of large segments of the piping system and

associated supporting structures. The type I vibrations are of high frequency (10-40 kHz) and are known as the "hoop" oscillation modes, experiments and data are given in Beltman and Shepherd (2002), Shepherd et al. (2008). The most severe type I vibrations are excited by the reflection of detonations in a compressed gas region when DDT takes place near the closed end or reflecting surface inside the piping system, this situation was examined previously (Liang et al., 2006) as a limiting case (PRC-DDT) (Ahnert, 2006b) for hazard estimation in WTP piping.

The type II vibrations can be further divided into bending, torsional, or longitudinal (axial) motions and various combinations. Since these vibrational modes result in the oscillation of large segments (1-10 m) of the piping system, they are usually referred to as "structural" oscillation modes. Due to the large mass and low stiffness in bending motions, the structural modes are of much lower frequency (10-1000 Hz) than the hoop modes. Although separated in frequency, the hoop and structural oscillations may be coincident in space and simultaneously contribute to the stresses at a given location in the piping system. Hoop and structural modes can overlap because: 1) the explosions are propagating waves that are continuously exciting the hoop oscillations at the detonation or shock front, 2) the structural vibrations propagate throughout the piping structure with a wide range of speeds, i.e., structural vibrations are dispersive and have no fixed phase speed. The fastest structural oscillation speeds are associated with the axial modes, which propagate with the bar speed, 5000 m/s, which is approximately twice the typical detonation speed of 2000 m/s. The structural oscillations are generated by impulsive reaction forces created when the pressure waves change in direction as they move through a piping system with bends, tees, dead ends and other typical features.

For example, a detonation wave propagating inside a tube with a bend (Fig. 1) creates an sudden unbalanced reaction force $F_b(t)$ due to the change in direction of the flow. The sudden reaction force generates axial forces along the two legs of the piping system connected to the bend and also bending moments on the segments of pipe connected to each end of the bend. The magnitude of the forces and moments and the resulting vibration amplitudes will depend on the flexibility of the bend (Rodabaugh, 2002) and stiffness of the piping segments. In commercial piping systems, the piping system will be supported by various means (Antaki, 2003) that will restrict the motion and also carry a portion of the structural load.

A key issue for piping designers that is currently outside of the piping design codes (ASME, 2001, Rao, 2002, 2006) and pressure vessel handbooks is how to treat detonation wave loading in the design process. While it is possible to use computational fluid dynamics (CFD) to estimate the internal load and computational solid dynamics (finite element

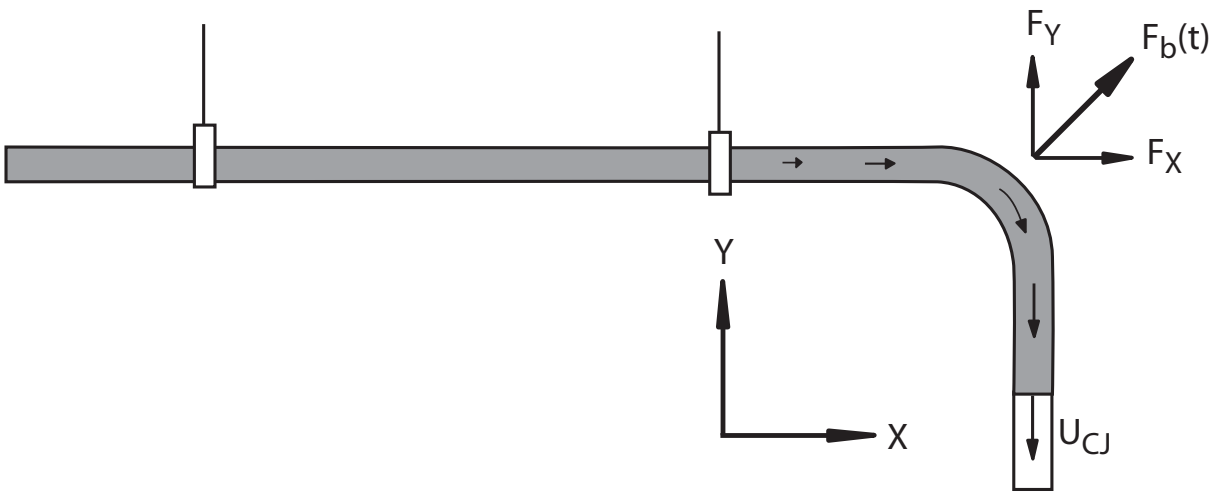

Figure 1: Detonation propagation in tube with a bend.

methods) to analyze a complete piping system, see Ahnert (2006a,c), this is very intensive in computing resources and personnel. Very little or no experimental data is available on the response of entire piping systems that could be used to validate such simulations. Thomas (2002) carried out experiments on a piping system constructed from GRP and MDPE, measuring strain, displacement, and pressure at selected points in three systems: a single bend, a double bend, and a tee. Ahnert (2006c) used a traveling load model of the detonation waves and a finite element model of the piping and supports to test the methodology developed to model detonations in the WTP piping. However, the results were inconclusive due to the very nonideal nature of the piping system and supports, resulting in significant difficulties in modeling and data interpretation.

More practical methods are sought that can be used for rapid hazard screening and design optimization. One method that is standard in the seismic and flexibility analysis of piping (Olson, 2002) is to represent the piping system as a space frame similar to the methods used in structural analysis. In order to use simplified structural models and computer programs like ME101, the forces at the bends, tees, and dead ends must be specified by the user. The purpose of the present study is to examine force-time models for one component, a single bend, under ideal detonation loading. This is just one part of a larger study considering other components and other types of explosive events.

2 Vibrations in Piping Systems

The hoop oscillations due to shock and detonation waves have been extensively studied (Beltman and Shepherd, 2002, Shepherd et al., 2008) and can be characterized by a frequency close to the radial oscillation frequency of the long, thin tube

$$f = \frac{1}{2\pi R}\sqrt{\frac{E}{\rho(1-\nu^2)}} \tag{1}$$

with a radius R, thickness h, Young's modulus E, and Poisson's ratio ν. For 2-in diameter schedule 40 stainless steel (type 304) pipe, see Table 2, the characteristic hoop frequency is 29 kHz. The largest strains are the hoop direction and the peak value can be estimated as

$$\epsilon_{\theta,max} = \Phi\frac{R}{h}\frac{\Delta P}{E}\ , \tag{2}$$

where Φ is the dynamic load factor, typically between 1 and 2 for commercial piping systems and $\Delta P = P_{max} - P_a$ is the difference between the maximum internal pressure and the external or ambient pressure. For propagating detonation waves, the maximum pressure is effectively the Chapman-Jouguet (CJ) value, 2.63 MPa for a H_2-N_2O mixture at 100 kPa initial pressure and room temperature, see Table 3. For elastic oscillations in steel piping systems, the hoop strain will be less than or equal to 2 $\times 10^{-3}$ or 2000 μstrain which means that the corresponding peak radial displacements $\delta_r = R\epsilon_\theta$ are on the order of 50 μm for the example 2-in pipe. The corresponding peak radial velocities will be 9.6 m/s^2 and the accelerations are 1.9×10^5 g (1.86×10^6 m/s^2.).

The structural oscillations of the piping system are associated with modes associated with the straight sections: beam bending, torsion, axial compression, radial-axial modes (Blevins, 1979), and also various coupled modes due to the bends, tees, and the three-dimensional nature of industrial piping systems.

The modes and frequencies for a simply supported 5.3-m long section of 2-in schedule 40 steel pipe are shown in Fig. 2. These were computed using the thin-wall tube analytical results of Blevins (1979) and previous experience with FEM models shows that the analytical results are adequate for describing the low-order modes of oscillations. The lowest frequency modes (the smallest is 5.5 Hz in this example) are the beam-bending modes and these are most likely to be excited by transient forcing. From beam theory, the oscillation frequencies are

$$f_i = \frac{\lambda_i^2}{2\pi L^2}\sqrt{\frac{EI}{M/L}}\ , \tag{3}$$

where M is the beam mass, L is the length, I is the area moment of inertia about the neutral axis, and λ_i is the mode frequency factor, which depends on the mode number i and boundary conditions. For a pinned-pinned beam (Blevins, 1979), these values are

$$\lambda_i = \pi i \qquad i = 1, 2, 3, \ldots \tag{4}$$

and the area moment of inertia for a pipe of inner radius R_i and outer radius R_o is

$$I = \frac{\pi}{4}\left(R_o^4 - R_i^4\right) \approx \pi R^3 h \; . \tag{5}$$

The lowest order bending mode frequency is therefore

$$f_1 = \frac{\pi}{2\sqrt{2}} \frac{R}{L^2} \sqrt{\frac{E}{\rho}} \tag{6}$$

which is a factor of R^2/L^2 smaller than the hoop frequency, explaining the 4 decade range in frequencies present in the mode plot of Fig. 2.

Introduction of bends or tee elements in the piping system introduces additional modes of vibration due to the coupling between beam, torsion, axial, and radial modes in these geometries. As an example consider the ES1 piping system tested at CIT, shown in Fig. 3. The first 20 modes as computed by a finite element model (FEM) of the piping system are shown in Table 1. The frequency range (11.6–557 Hz) overlaps that (5.5-479 Hz) for the lowest frequencies of the principal modes (except pure radial motion at 29 kHz) of a straight pipe of the same total length (207 in or 5.3 m) shown in Fig. 2. Examination of the modal geometry reveals that the lowest frequency mode for the case of a bend corresponds to an out-of-plane bending motion with the elbow moving perpendicular to the plane of the bend. The bend creates a significant difference in stiffness for in-plane and out-of-plane motion with much less resistance to out-of-plane motion than in-plane vibration.

The total number of modes less than a given frequency depends on the choice of azimuthal wave number for the analytical results (Fig. 2) and the resolution (number of elements) for the FEM model. In the case of the analytical model, we have arbitrarily cut off the azimuthal wave number at 8 to avoid cluttering the plot. For detonation loading, a mix of high and low frequency modes will be excited with the highest frequency radial mode excited by the sudden application of high pressure behind the moving detonation wave and lower frequency modes being excited due to the forces on closed ends, bends and tees. One of the key issues in analyzing detonations in piping systems is the extent of superposition of these modes and how this should be accounted for in the analysis.

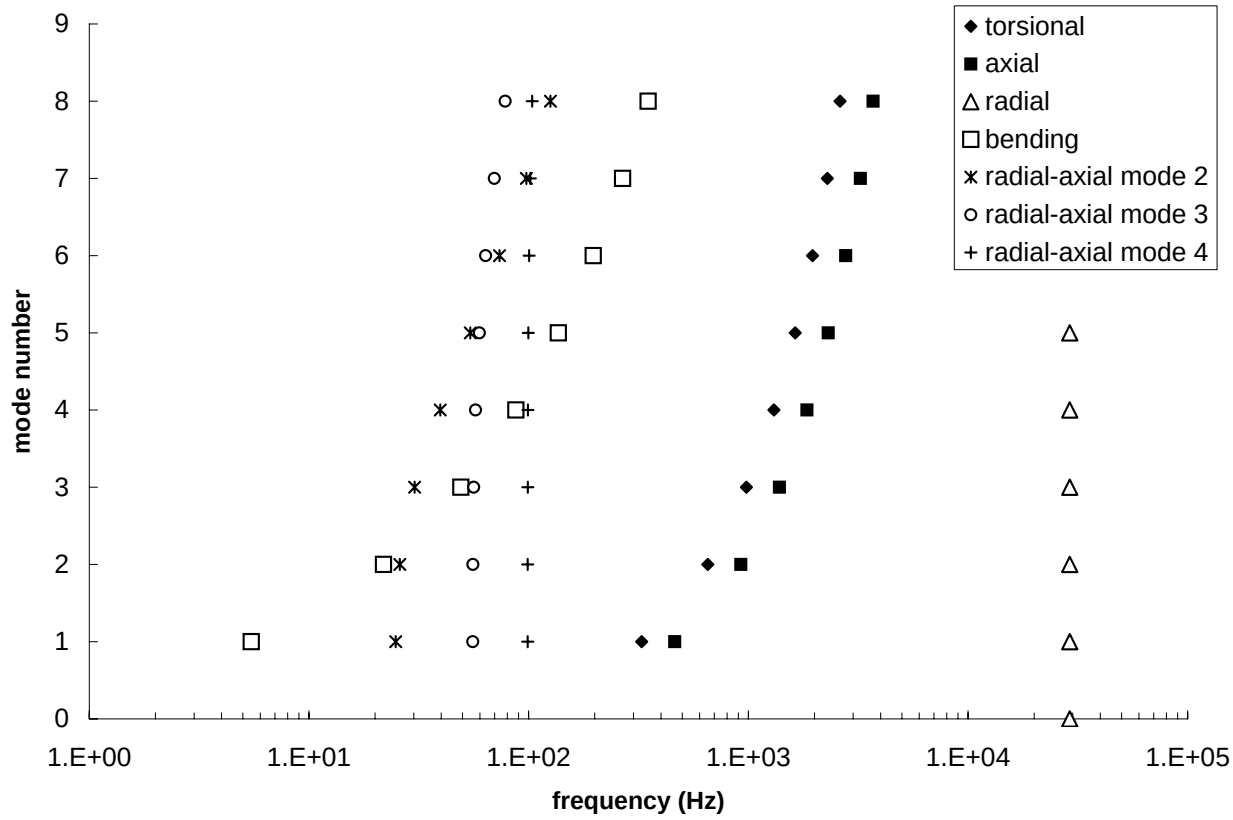

Figure 2: Vibrational frequencies for a 5.3-m section of 2-in schedule 40 pipe with simply supported ends.

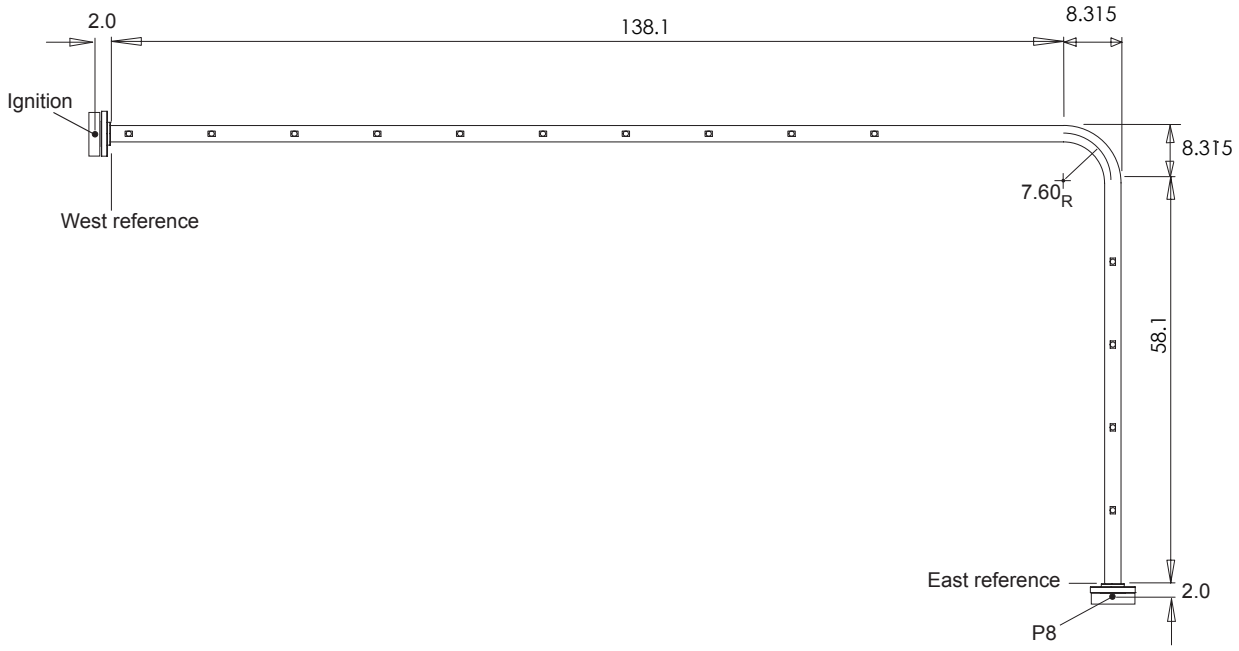

Figure 3: Schematic layout and overall dimensions (inch) of the ES1 specimen constructed from Schedule 40, 304 Stainless steel pipe.

Table 1: First 20 vibrational mode frequencies of the ES1 specimen (fixed ends) as computed by ANSYS (Preliminary results by Tom Ligon of DEI) using shell elements.

Mode	Frequency (Hz)
1	11.593
2	21.788
3	26.867
4	60.827
5	64.224
6	100.33
7	103.1
8	133.23
9	140.07
10	209.71
11	214.41
12	278.76
13	288.1
14	317.58
15	342.07
16	359.77
17	404.18
18	440.62
19	448.77
20	556.67

3 Detonation Propagation in a Bend

The interaction of shock (Edwards et al., 1983, Henshaw et al., 1986) and detonation (Williams and Thomas, 2002) waves with bends is characterized by two competing effects, expansion waves created by diffraction as the wave moves along the convex surface of the intrados and compression waves created as the wave moves along the concave surface of the extrados. The results are simpler to understand for shock waves since there is no interaction with the chemical reaction process. As discussed by Edwards et al. (1983) and Henshaw et al. (1986), the shock wave slows as it moves along the intrados and speeds up on the extrados. The expansion waves create a smooth curved wave front along the intrados but compression waves create a strong shock (Mach stem) on the extrados with a sharp kink where the strong wave joins the main wave front. The result is that initially planar wave front emerges from the bend with a non-planar shape. An example is shown in Fig. 4.

For this case, the distortion of the wavefront within the bend is clear but the front returns to a nearly planar shape at the exit of the bend. At a given angular location along the bend, the wave has further to travel along the outside than the inside so that initially the outer portion of the wave appears to lag behind the inner. Aa wave speed increases on the outside and decreases on the inside, the situation is reversed and the outer portion of the wavefront emerges from the bend before the inner portion. The extent of non-planarity and the shape of the emerging shock front depends on the sharpness of the bend and for smaller radius bends the wavefront can be quite distorted when it emerges from the bend (Henshaw et al., 1986).

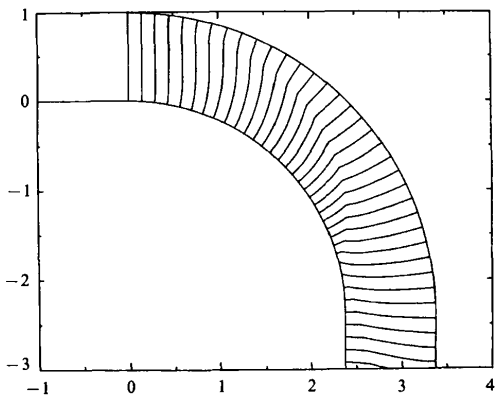

Figure 4: Simulation of shock wave diffracting through a 90-degree bend in a two-dimensional channel. The shock wave Mach number at the channel entrance (upper left) is 1.9 and the bend radius is approximately 3 channel widths. From Henshaw et al. (1986).

The diffraction of a detonation wave is more complex due to the strong coupling of the

rate of chemical reaction to the strength of the leading shock front (Shepherd et al., 2000). On the outer wall, the shock wave accelerates, the post shock temperature increases, and the chemical reaction rate increases - this simply results in a thinner reaction zone and a more ideal detonation. On the inner wall, the shock wave slows, the post shock temperature decreases, and the reaction rate drops. If the reaction rate drops too quickly, the reaction can be quenched and the detonation wave speed will rapidly drop. Once the wave emerges from the bend, chemical reaction may be reestablished behind the low speed wave due to interaction with the strong Mach stem propagating from the extrados toward the intrados, as shown in Fig. 4. The extent of this effect and the relevance to bend force prediction depend strongly on the reactivity of the combustible mixture and the radius of the bend. For highly reactive and large radius bends, the effect will be smaller than for low reactivity mixtures propagating through a small radius bend.

The behavior of a low-reactivity-mixture detonation in a bend is illustrated by the simulation results of Deiterding (2006, 2007), who computed the propagation of detonation in a $2H_2+O_2+7Ar$ mixture at 6.7 kPa through a two-dimensional channel bend of 60°. The chemical reactions were modeled with a detailed kinetic mechanism and the reaction zone was sufficiently well resolved that a cellular structure was present on the front with a cell size of approximately 3 cm. The channel was 5λ wide and the radius of the bend was 9.375λ.

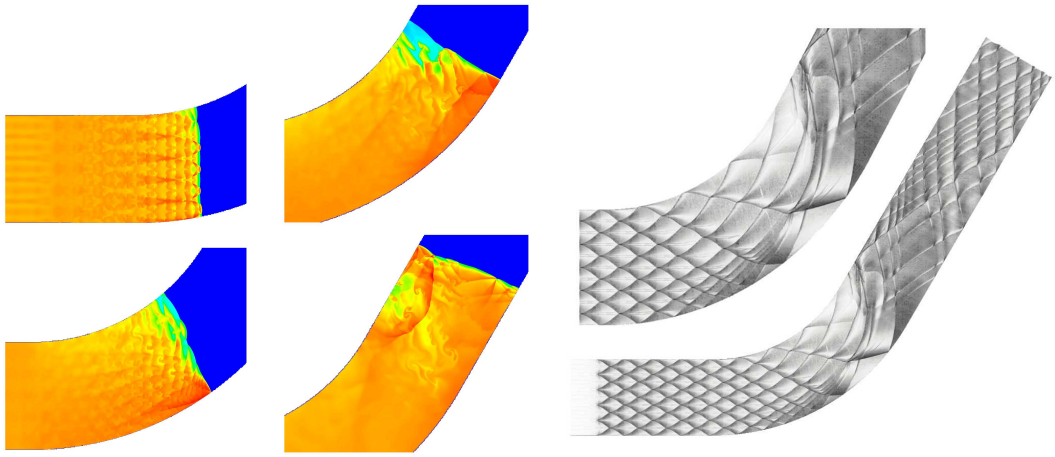

Figure 5: Simulations of detonation propagating through a gradual 60-degree bend in a tube. a), b) temperature contours. c) simulated soot foil. From Deiterding (2006).

The detonation enters the channel with the characteristic cellular structure typical of Ar-diluted hydrogen-oxygen mixtures (top plot of Fig. 5a) and a low temperature region is created along the intrados and a high temperature region is observed at the extrados (bottom plot of Fig. 5a and top plot of Fig. 5b). The transverse shock visible in the top plot of Fig. 5b

apparently re-initiates the detonation and a blast wave can be observed propagating away from the newly reacted region on the intrados in the bottom plot of Fig. 5b. In the soot track images of Fig. 5c the loss of the transverse wave structure within the bend can be seen in the top plot and the re-emergence downstream can be seen in the bottom plot. Williams and Thomas (2002) present experimental soot foils which show that the cellular structure can be maintained throughout the bend if the mixture is sufficiently reactive and the channel radius sufficiently large. Williams and Thomas (2002) also present pressure measurements obtained in bends fabricated from 300 mm diameter GRP piping used in the system tests described in Thomas (2002). These measurements were inconclusive but support the idea that higher pressures were present on the extrados than on the intrados in those tests.

An extensive study of the pressures and strains due to a detonation propagating in a 90-degree bend within a metal tube was carried out by Liang et al. (2008a,b). Two examples of the pressure traces obtained in that study are shown in Fig. 6. A detailed presentation and analysis of the pressure and strain histories can be found in Liang et al. (2008b). For highly reactive mixtures, the detonation is observed to speed up on the extrados but does not significantly slow down on the intrados. The general shape of the pressure signals within the bend are similar to those measured for a detonation wave in a straight channel but with additional high frequency disturbances and spikes near the front. The maximum amplitude of the hoop strains on the bend was found to be similar to those measured on straight tubes.

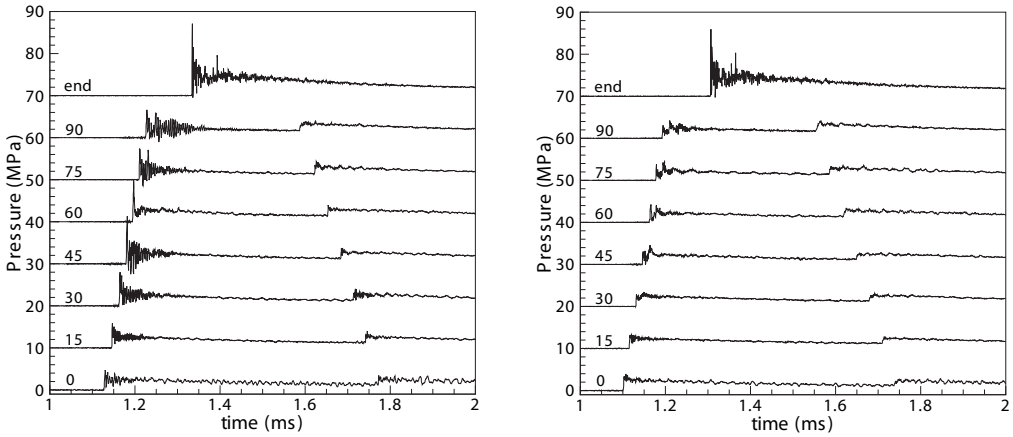

Figure 6: Pressure measurements on a detonation propagating through a gradual 90-degree bend in a tube. a) intrados. b) extrados. Liang et al. (2008a,b)

4 Bend Force Analysis

We consider several approaches to estimating the force history $F(t)$ associated with detonation propagation through the bend. The fundamental idea is to apply the control volume approach to the momentum equation

$$\frac{d}{dt}\int_{\Omega}\rho\vec{u}\,dV = \vec{R} - \int_{\partial\Omega}\rho\vec{u}\vec{u}\cdot\hat{n}dA - \int_{\partial\Omega}P\hat{n}\,dA \tag{7}$$

using one of the control volumes Ω with surface area $\partial\Omega$ shown in Fig. 7. In writing this momentum balance, we have assumed that the bend is rigid and stationary. For thick-walled, gas-filled piping systems that respond elastically, this is a reasonable approximation at early times. Large deformations of the piping system may occur but these typically take place on longer time scales (10–100 ms) compared to the wave motion and gas flow within the bend (0.1–1 ms). The deformations of a bend or elbow are important in determining the flexibility of the bend or elbow due to *ovalization* of the pipe and will contribute to the coupling of the deformation modes. This is not treated by the present approach, for a discussion of flexibility factors, see Rodabaugh (2002).

In computing the traction forces on the boundaries, the shear stress forces created by the fluid motion are neglected in comparison to the pressure forces. The gas flows are transient and the pressures in detonations or strong shock waves are sufficiently large that they will completely dominate the contribution of shear stresses. The usual convention in mechanics is used in assigning a reaction force $\vec{R} = \vec{R}_1 + \vec{R}_2$ on the bend to keep it stationary. The reaction forces are shown at the entrance (1) and exit (2) of the bend in Fig. 7a. If we apply the reaction force as a point load as shown in Fig. 7c, then we should also specify a moment to be consistent with the distributed reaction forces. We have not considered the moments in this discussion. We rewrite the momentum equation to explicitly show the two contributions to the force $\vec{R}$.

$$\vec{R} = \underbrace{\int_{\partial\Omega}\left[\rho\vec{u}\vec{u}\cdot\hat{n} + P\hat{n}\right]\,dA}_{steady} + \underbrace{\frac{d}{dt}\int_{\Omega}\rho\vec{u}\,dV}_{unsteady} \tag{8}$$

If we use the control volume $\mathcal{O}$ shown in Fig. 7, the internal pressure and fluid motion motion at the inlet (1) and exit (2) of the bend contribute to the "steady" integral. Outside of the pipe, the ambient pressure P_a in the atmosphere contributes to the "steady" integral. Filling or emptying of the bend with fluid or more generally, any change of mass and/or fluid velocity within the bend will contribute to the "unsteady" integral. The first or "steady" integral will contribute to the force in both unsteady and steady situations but the second

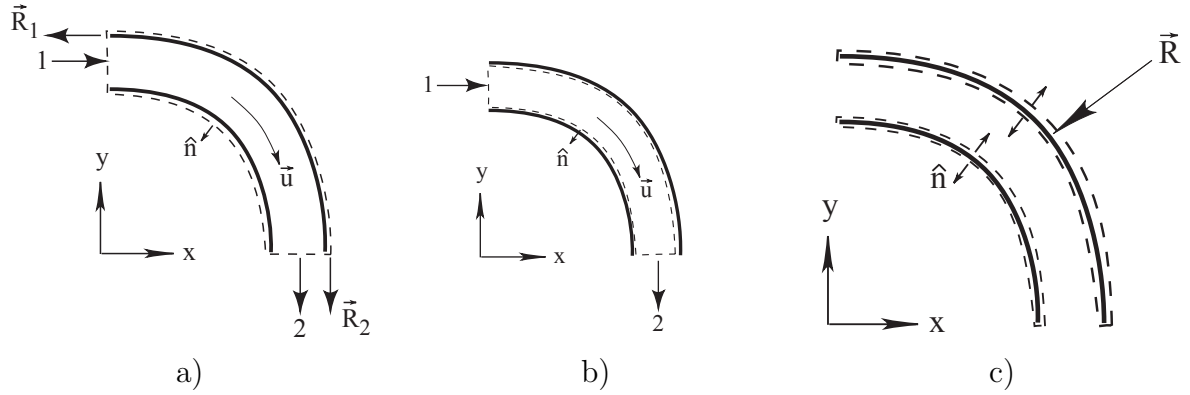

Figure 7: Control volumes used to analyze a detonation propagating through a bend. a) $\mathcal{O}$ - contains both pipe and fluid. b) $\mathcal{I}$ - contains only fluid. c) $\mathcal{P}$ - containing only the pipe. This is equal to the difference of $\mathcal{O}$ and $\mathcal{I}$.

or "unsteady" integral will only contribute if there is significant unsteadiness in the flow. The control volume approach to analyzing forces on piping and vessels as well as numerous applications to unsteady situations is presented in the textbook by Moody (1990).

4.1 Interpreting the Reaction Force

The reaction force can be interpreted in terms of the surface forces that act on the pipe. Consider the control volume $\mathcal{P}$ surrounding just the pipe as shown in Fig. 7c. There is no fluid flowing through this control surface so that the force can be computed from pressures acting on the interior and exterior of the pipe. Since at a point on the pipe the interior and exterior pressure act in opposite directions, the integration over the control surface $\mathcal{P}'$ can be simplified by supposing the pipe has no thickness, i.e., that the inside and outside of the control surface are coincident. The integral can therefore be carried out over a single surface representing the pipe and labeled $\mathcal{P}'$.

$$\vec{R} = -\int_{\partial\Omega_{\mathcal{P}'}} (P(\vec{x},t) - P_0)\,\hat{n}\,dA\,. \tag{9}$$

The pressure $P(\vec{x},t)$ is the pressure inside the pipe, and the surface normal $\hat{n}$ is directed outward, i.e., pointing from the interior to the exterior of the pipe. As expected, we see that the reaction force is equal and opposite the force $\vec{F}$ created by the unbalanced pressures on the inside of the bend

$$\vec{R} = -\vec{F} \tag{10}$$

where

$$\vec{F} = \int_{\partial\Omega_{\mathcal{P}'}} (P(\vec{x},t) - P_0)\,\hat{n}\; dA\;. \tag{11}$$

The force $\vec{F}$ can also be written in terms of the steady and unsteady momentum integral contributions (8) as

$$\vec{F} = -\int_{\partial\Omega} \left[\rho\vec{u}\vec{u}\cdot\hat{n} + P\hat{n}\right]\; dA - \frac{d}{dt}\int_{\Omega} \rho\vec{u}\; dV \tag{12}$$

For the remainder of the discussion, we will calculate the fluid force $\vec{F}$ rather than the reaction force $\vec{R}$. The expression (11) is deceptively simple since unless the pressure $P(\vec{x},t)$ is known everywhere on the interior surface as a function of time, we cannot evaluate the integral. The integrals in (12) are actually easier to use since they only require estimating the flow at the entrance and exit of the bend and the unsteady motion of the detonation within the bend.

4.1.1 Previous Work

An approximation that is often used in piping vibration analysis (see Fig. 37.2 of Olson, 2002) is that the pressure is spatially uniform within the bend, $P(\vec{x},t) = P_i$. The surface integral can be evaluated explicitly using the simple trick that the integral of a constant vector $\Delta P = P_i$ - P_a over a closed surface vanishes

$$0 = \int_{\partial\Omega_O} \Delta P\hat{n}\; dA \tag{13}$$

The surface $\partial\Omega_{\mathcal{O}} = \partial\Omega_{\mathcal{P}'} + \partial\Omega_1 + \partial\Omega_2$. Computing the integral over these three areas, we find that the sum of the contributions over the ends are equal and opposite to the contribution over the exterior surface of the pipe

$$\int_{\partial\Omega_{\mathcal{P}'}} \Delta P\hat{n}\; dA = -\int_{\partial\Omega_1} \Delta P\hat{n}\; dA - \int_{\partial\Omega_2} \Delta P\hat{n}\; dA\;. \tag{14}$$

The surface integrals over the end areas Ω_1 and Ω_2 can be easily carried out to give

$$\vec{F} = \hat{x}A\Delta P + \hat{y}A\Delta P \tag{15}$$

where A is the crossection area of the pipe. The magnitude of the force for a 90° bend is

$$|\vec{F}| = \sqrt{F_x^2 + F_y^2} \tag{16}$$

$$= \sqrt{2} A \Delta P \tag{17}$$

For a bend through an angle $\Delta\theta$ (this is the angle that the fluid turns) that is other than 90°, the force will be directed outward, from the intrados to the extrados of the bend, em along the line that bisects the arc between the inlet and exit planes, see Fig. 8. For the geometry shown in the figure with the flow entering the bend on the $+x$ direction, the force can be found by trigonometry to be

$$F_x = A\Delta P(1 - \cos\Delta\theta) \ , \tag{18}$$

$$F_y = A\Delta P \sin\Delta\theta \ , \tag{19}$$

and the magnitude of the force is

$$|\vec{F}| = \sqrt{2} A \Delta P \sqrt{1 - \cos\Delta\theta} \ . \tag{20}$$

Olson (1991) describes the application of this approach to estimating unbalanced loads on piping systems induced by pump oscillations or water hammer induced by valve operation. The forces at each bend are evaluated by using (20) with a time-dependent pressure $P(t)$ that accounts for the propagation of pressure pulses through the piping system but ignores the variation within each bend. This approximation is limited to situations where the flow speed is low enough that the spatial pressure variations within the bend can be neglected and the distance between bends is sufficiently large that the temporal variation within the bend can be neglected compared to the propagation delay between the bends. A related approach that is approximate but easier to use is to use the control volume $\mathcal{O}$ of Fig. 7a in order to avoid computing the pressure integral over the pipe. This will require approximating both the momentum flux at the inlet and exit of the control volume as well as the unsteady integral. We will discuss this approach next.

An approximate traveling load representation of a detonation wave was used to compute the forces on support loads for a representative WTP piping system in Ahnert (2006a). More refined estimates of forces on bends due to detonations were carried out (Gross and Minchello, 2007) by evaluating (11) using the pressure predicted by a computational fluid dynamic model of a detonation wave diffracting through a bend. These computations showed that there is a significant "asymmetry factor" associated with the temporal and spatial

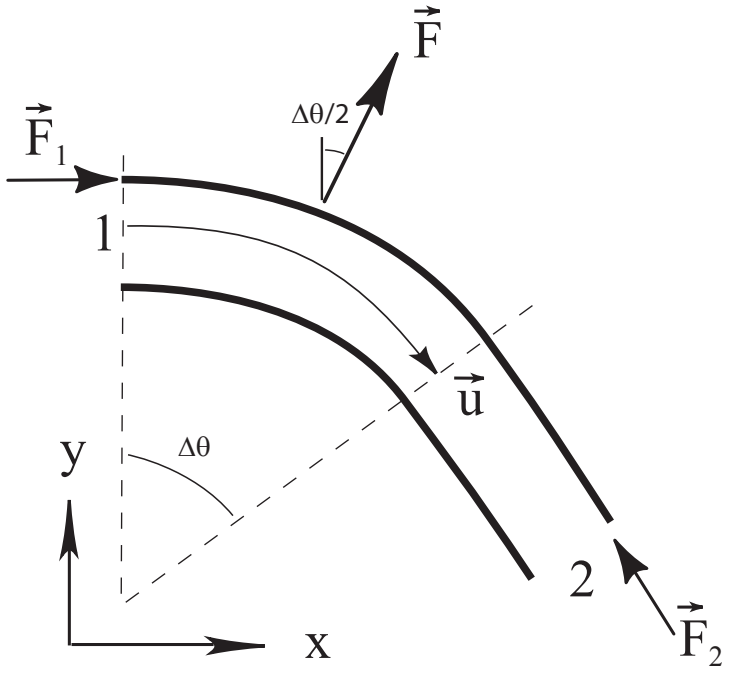

Figure 8: Forces on an arbitrary angle bend containing fluid in steady flow.

variation of pressure through the bend and that the approximate approach (20) usually used in piping analysis will not work for detonations. The reason for this failure is primarily due to the large pressure variations associated with the compressible high-speed flow behind the detonation wave. Based on the integration of the CFD results, a modification of the traveling load model of a detonation wave was proposed (Ligon, 2008), to approximately account for these variations using a parametric representation of the pressure rather than the results of a specific computational fluid dynamic approach. Using this parametric approach, simulations were performed to validate the predicted strains against detailed measurements in a 90-degree bend. On the basis of these results, a variation of the pressure asymmetry with azimuthal angle was proposed to bring the simulated strains into better agreement with the test results. A version of this methodology is proposed below. For the purpose of piping vibration analysis with a simple piping structural simulation, the goal to develop a function $\vec{F}(t)$ that can be applied as an external point load

$$\vec{F} = \hat{x}F_x(t) + \hat{y}F_y(t) \tag{21}$$

and simulates the forcing of vibration by the detonation passing through a bend.

4.2 Momentum Theorem Integral Estimation of Forces

Now consider the approach of using control volume $\mathcal{O}$ to find the force. Using the same approach as in (14) to evaluate the integrals on the exterior of the pipe, the "steady" integral of (8) can be rewritten in terms of integrals over the surfaces $\partial\Omega_1$ and $\partial\Omega_2$. On surface $\partial\Omega_1$, $\hat{n}$ = -$\hat{x}$ and on $\partial\Omega_2$, $\hat{n}$ = -$\hat{y}$ so that we can express the bend force as

$$\vec{F} = \int_{\partial\Omega_1} [\rho\vec{u}\vec{u}\cdot\hat{x} + (P - P_a)\hat{x}]\ dA + \int_{\partial\Omega_2} [\rho\vec{u}\vec{u}\cdot\hat{y} + (P - P_a)\hat{y}]\ dA - \frac{d}{dt}\int_{\Omega_O} \rho\vec{u}\ dV \quad (22)$$

First, we estimate the magnitude of the unsteady integral contribution to the reaction force. The problem of detonation propagation in a bend is obviously unsteady when the wave front is within the bend. Once the wave front has passed completely through the bend, a flow is set up within the bend that contributes to the steady integral with a time-dependent pressure and velocity. For a detonation wave started at the closed end of a pipe or channel, the unsteadiness in the flow behind the wave will depend on the distance that the detonation has propagated from the initiation point, see the subsequent discussion on the Taylor-Zeldovich flow behind ideal detonations. If there is a sufficiently large distance of propagation upstream of the bend, then we may be able to consider the flow through the bend as quasi-steady. This will greatly simplify the estimation of the forces on the bend.

4.2.1 Unsteady Contribution

The entire flow field following a detonation is unsteady so it is necessary to be precise about which unsteady contribution we are computing in this section. There are two origins of unsteadiness. First, unsteadiness arises when the detonation wave propagates through the bend segment of the piping. Second, pressure, density and flow velocity behind the detonation front are unsteady due to the Taylor-Zeldovich expansion wave behind the detonation front. This results in unsteady changes in density and flow velocity within the bend during and after the detonation front has passed through the bend, However, if the straight section upstream of the bend is long compared to the distance the wave front has to travel within the bend, the unsteadiness in the flow behind the front occurs over a much longer time scale than that associated with the wave front propagation through the bend. This insures that the dominate contribution of the unsteadiness arises from the propagation of the front within the bend and otherwise the forces arise due to the steady or more strictly speaking, quasi-steady contributions alone.

To see this, we will first make an order of magnitude estimate of the unsteady contribution to the forces when the detonation is within the bend. We will assume the properties behind

the wave front are constant and approximately the CJ state. Assuming a 90-deg bend with radius R, we estimate the time scale of the flow changes as $\pi R/(2U_{CJ})$, and the magnitude of the unsteady contribution to the force due to propagation within the bend is

$$-\frac{d}{dt}\int_{\Omega_O}\rho\vec{u}\,dV \sim -\frac{\rho_{CJ}u_{CJ}A\pi R/2}{\pi R/(U_{CJ})} \tag{23}$$

$$\sim -\rho_{CJ}u_{CJ}U_{CJ}A\,. \tag{24}$$

Next, we will make an estimate of the unsteady forces after the detonation front has passed through the bend. Estimating the time scale of flow changes as L/U_{CJ}, where L is the distance from the previous bend or initiation point, the unsteady contribution will be

$$-\frac{d}{dt}\int_{\Omega_O}\rho\vec{u}\,dV \sim -\rho_{CJ}u_{CJ}U_{CJ}A\frac{\pi R}{2L} \tag{25}$$

which is a factor of R/L smaller than the unsteadiness associated with the propagation through the bend. As long as $L >> R$, we can neglect the second source of unsteadiness. This is typically the case since the wave front is inside the bend for only a short time compared to the time time of wave propagation between the bends. For example, in a 3-diameter radius bend in 2-in pipe, the wave transit time through the bend is 0.12 ms while the typical wave transit time between bends will be 2 ms for a bend spacing of 4 m. The initial magnitude of the steady contribution to the force is estimated as

$$\int_{\partial\Omega}\left[\rho\vec{u}\vec{u}\cdot\hat{n}+P\hat{n}\right]\,dA \sim A\left[P_{CJ}-P_a+\rho_{CJ}u_{CJ}^2\right], \tag{26}$$

From the values of CJ properties in Table 3, we compute that

$$\rho_{CJ}u_{CJ}U_{CJ} = 4.27 \text{ MPa} \tag{27}$$

and

$$P_{CJ}-P_a+\rho_{CJ}u_{CJ}^2 = 4.64 \text{ MPa} \tag{28}$$

showing that the magnitude of the unsteady term is comparable to the steady term while the wave front is within the bend.

In order to make a more precise estimate of the unsteady integral while the detonation front is within the bend, we need to simplify the description of the flow field by idealizing

the detonation wave as a planar front that moves at the velocity U and is followed by a flow with speed (lab frame) of u and density ρ. The geometry is shown in Fig. 9 To evaluate

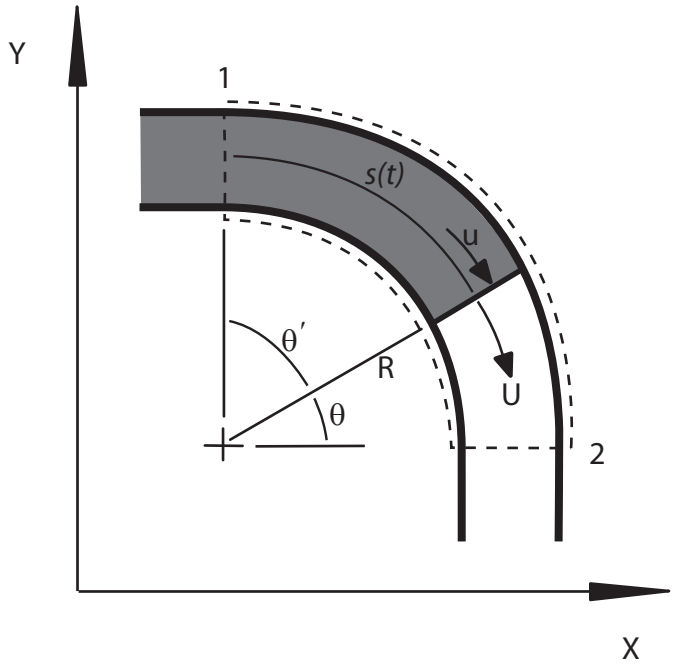

Figure 9: Control volume used to analyze unsteady contribution to force created by a detonation propagating through a bend. Shaded area represents products of combustion moving behind the detonation front.

the unsteady integral, we will further assume that the detonation front moves at a constant speed U on a circular arc of radius R and the following flow has a speed u with stream lines that are circular arcs of radius R. The arc length s of the streamline as measured from plane 1 is (Fig. 9)

$$s(t) = U(t - t_1) \tag{29}$$

where t_1 is the time that the detonation reaches plane 1. We will assume circular arc streamlines and uniform flow across the cross-section of the pipe, so that the velocity can be written as

$$\vec{u}(s) = u(\theta', t)\left[\hat{x}\cos\theta' - \hat{y}\sin\theta'\right] \tag{30}$$

where $\theta' = \pi/2$ - θ is defined in Fig. 9. The arc length is related to the complement angle through

$$s = R\theta' \tag{31}$$

so that

$$\theta' = \frac{s}{R} \tag{32}$$

With these assumptions and definitions, the unsteady contribution can be written as

$$-\frac{d}{dt}\int_{\Omega_O} \rho\vec{u}\, dV = -A\frac{d}{dt}\int_0^{s(t)} \rho(s',t)\vec{u}(s',t)\, ds' \tag{33}$$

Appyling Liebniz's rule to carry out the differentiation, we find that

$$-\frac{d}{dt}\int_{\Omega_O} \rho\vec{u}\, dV = -A\rho(s,t)\vec{u}(s,t)U + \int_0^{s(t)} \frac{\partial}{\partial t}\left[\rho(s',t)\vec{u}(s',t)\right]\, ds' \tag{34}$$

The assumption that we are making in this section is the the second term is negligible compared to the first. The gives the approximate unsteady contribution of

$$-\frac{d}{dt}\int_{\Omega_O} \rho\vec{u}\, dV \approx -A\rho\vec{u}U \tag{35}$$

$$\approx \rho u A U\left[-\hat{x}\cos\left(\frac{U(t-t_1)}{R}\right) + \hat{y}\sin\left(\frac{U(t-t_1)}{R}\right)\right] \tag{36}$$

for the time that the detonation front is in the bend

$$t_1 < t < t_2 = t_1 + \frac{R\Delta\theta}{U} \tag{37}$$

The unsteady effect can be roughly accounted for by applying an impulse to the bend at the time of detonation wave transit. The impulse is approximately

$$\vec{I} = \int_{t_1}^{t_2} \vec{F}_{unsteady}(t)\, dt \tag{38}$$

$$= \rho_{CJ}u_{CJ}AR\int_0^{\pi/2}\left[-\hat{x}\cos\theta' + \hat{y}\sin\theta'\right]\, d\theta' \tag{39}$$

$$= \rho_{CJ}u_{CJ}AR\left[-\hat{x} + \hat{y}\right] \tag{40}$$

which is oriented tangentially to the bend opposite to the direction of flow.

4.2.2 Steady Contribution

Now we consider the steady flow integral contribution to the momentum balance. From (22) with the unsteady term omitted, we have

$$\vec{F} = \int_{\partial\Omega_1} \left[\rho\vec{u}\vec{u}\cdot\hat{x} + (P - P_a)\hat{x}\right]\, dA + \int_{\partial\Omega_2} \left[\rho\vec{u}\vec{u}\cdot\hat{y} + (P - P_a)\hat{y}\right]\, dA\,. \tag{41}$$

Assuming that the flow profile at the inlet and exit is spatially uniform (sometimes called a top-hat profile), the bend force will be

$$\vec{F} = \hat{x}A_1\left[(P_1 - P_a) + \rho_1 u_1^2\right] + \hat{y}A_2\left[(P_2 - P_a) + \rho_2 u_2^2\right]\,, \tag{42}$$

a result that is also often used in piping vibration analysis (See Eq. 29.22 Blevins, 2002) with constant values for P, ρ and u. In our case, these values depend on time. Our analysis shows that in order to rigorously extend (42) to time-dependent flows, we also need to consider the truly unsteady contribution to the momentum theorem discussed in Section 4.2.1. We will see that in some situations, it is possible to make a quasi-steady approximation and use unsteady quantities in the momentum flux terms (42) but neglect the contributions of the unsteady or storage integral. This is considered in the final evaluation of the momentum theorem model presented in Section 5.2.

4.3 Summary of Momentum Theorem Integral Model

Combining the approximate quasi-steady (42) and unsteady contributions (36) to the momentum theorem, our approximation to the bend forces for a constant cross-section bend can be written as

$$\begin{aligned}\vec{F}(t) = {} & \hat{x}A\left[(P_1(t) - P_a) + \rho_1(t)u_1^2(t)\right] + \hat{y}A\left[(P_2(t) - P_a) + \rho_2(t)u_2^2(t)\right] \\ & + \rho_{CJ}u_{CJ}U_{CJ}A\left[-\hat{x}\cos\left(\frac{U(t-t_1)}{R}\right) + \hat{y}\sin\left(\frac{U(t-t_1)}{R}\right)\right]\end{aligned} \tag{43}$$

for the time that the detonation front is in the bend

$$t_1 < t < t_2 = t_1 + \frac{R\Delta\theta}{U}$$

and

$$\vec{F}(t) = \hat{x}A\left[(P_1(t) - P_a) + \rho_1(t)u_1^2(t)\right] + \hat{y}A\left[(P_2(t) - P_a) + \rho_2(t)u_2^2(t)\right]$$

for times $t > t_2$ after the detonation has passed through the bend. The functions $P(t)$, $\rho(t)$, and $u(t)$ have not been determined at this point but we propose subsequently (Section 5) to use values obtained from the ideal detonation flow field based on the Taylor-Zeldovich similarity solution.

4.4 Pressure variation within bend

Finally, consider using the control volume $\mathcal{I}$ to evaluate the momentum integral for the case of steady or quasi-steady flow. There are no external forces so that integrals can be written

$$\int_{\partial\Omega_{\mathcal{I}}} \rho\vec{u}\vec{u}\cdot\hat{n}dA = -\int_{\partial\Omega_{\mathcal{I}}} P\hat{n}\ dA \tag{44}$$

Since the velocity normal to the pipe surface must be zero for a rigid pipe, the left-hand side only has contributions from the surfaces at the end of the control volume. We can therefore express the pressure integral over a closed surface in terms of the integrals of the flux $\rho\vec{u}\vec{u}\cdot\hat{n}$ through the ends.

$$\int_{\partial\Omega_{\mathcal{I}}} P\hat{n}\ dA = \int_{\partial\Omega_1} \rho\vec{u}\vec{u}\cdot\hat{x}dA + \int_{\partial\Omega_2} \rho\vec{u}\vec{u}\cdot\hat{y}dA \tag{45}$$

This shows that if the flux integrals are nonzero, then there must be a spatial variation of pressure within the bend since the integral of a constant pressure over a closed surface is zero, leading to the contradiction. We conclude that when there is significant fluid motion inside the pipe, a realistic representation of the pressure must have a spatial variation within the bend in order for the forces to be consistent with the conservation of momentum. This is important to keep in mind when constructing "traveling load" pressure distributions to apply to the interior of finite-element models of piping systems.

In order to integrate the pressure, we will use the toroidal co-ordinate system shown in Fig. 10 to evaluate the integral of (11) with the quasi-steady representation of

$$P(t,\theta,\phi) = P_a + \Delta P(t) \times f(\theta,\phi)\ . \tag{46}$$

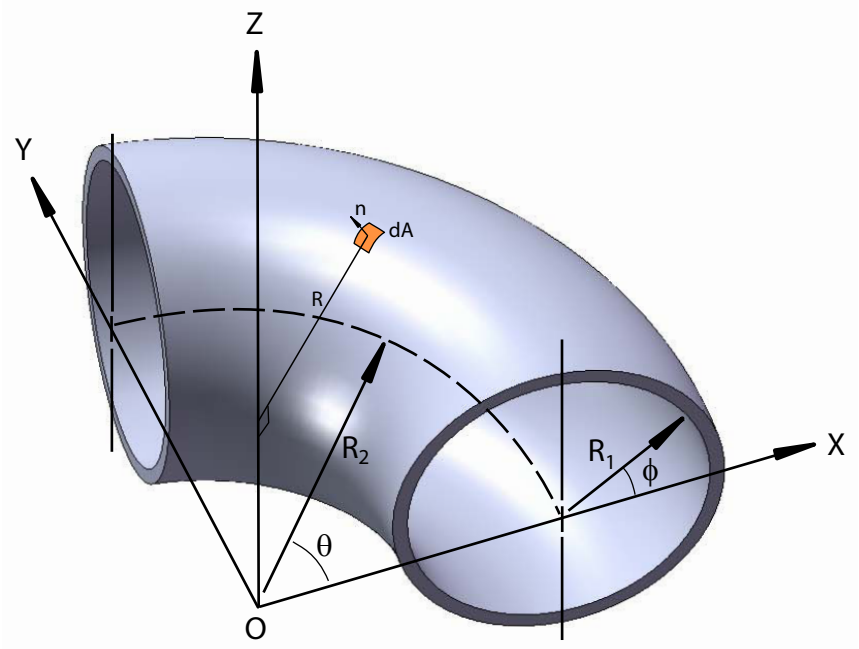

Figure 10: Geometry of bend surface and area element used to integrate pressure to obtain the force.

where $\Delta P(t)$ is the average difference in internal and external pressure at the inlet or exit of the bend. Ultimately, the ideal Taylor-Zeldovich flowfield described in Section 5 will be used to evaluate this function. With these defintions, the components of force are

$$F_x = \Delta P(t) \int \int n_x f(\theta, \phi)\, dA \tag{47}$$

$$F_y = \Delta P(t) \int \int n_y f(\theta, \phi)\, dA \tag{48}$$

and F_z is assumed to be zero by construction, which requires that $f(\theta, \phi) = f(\theta, -\phi)$. The normal vector components can be computed from the pipe bend geometry assuming that it is generated by a circle of radius R_1 (the pipe innner diameter) rotated about the z axis with the center of the circle at the bend radius R_2.

$$n_x = \cos\phi \cos\theta \tag{49}$$

$$n_y = \cos\phi \sin\theta \tag{50}$$

$$n_z = \sin\phi \tag{51}$$

The perpendicular distance R from the z axis to the surface of the pipe is

$$R = R_2 + R_1 \cos\phi \tag{52}$$

The element of surface area is

$$dA = R_1 R \, d\phi \, d\theta \tag{53}$$

Substituting these expressions, we obtain the final result in terms of the integration in angle where the limits have been chosen to correspond to a 90° bend but can be readily generalized.

$$F_x = \Delta P(t) \int_o^{\pi/2} \int_{-\pi}^{+\pi} f(\theta,\phi) \, \cos\phi \cos\theta \, R_1 (R_2 + R_1 \cos\phi) \, d\phi \, d\theta \tag{54}$$

$$F_y = \Delta P(t) \int_o^{\pi/2} \int_{-\pi}^{+\pi} f(\theta,\phi) \, \cos\phi \sin\theta \, R_1 (R_2 + R_1 \cos\phi) \, d\phi \, d\theta \tag{55}$$

The function f has several constraints other then being an even function of ϕ. It should be unity at the ends of the bend

$$f(\theta = 0, \phi) = 1 \tag{56}$$

$$f(\theta = \pi/2, \phi) = 1 \tag{57}$$

and the circumferential (ϕ) average value should be unity

$$1 = \frac{1}{2\pi} \int_{-\pi}^{+\pi} f(\theta,\phi) \, d\phi \; . \tag{58}$$

Both of these constraints will enable the result to smoothly blend with the solution for a straight pipe upstream and downstream of the bend and approach the result for a straight pipe uniformly as the bend radius R_2 approaches ∞.

The function $f(\theta,\phi)$ is an extremely approximate representation of the pressure field. Even if our flow were truly steady and incompressible, there are a number of complications resulting from flow around a bend (Berger et al., 1983), notably the creation of a secondary flow (perpendicular to the main flow direction) upstream of and within the bend and the Rayleigh instability of the boundary layer on the outer wall of the pipe (Vanyo, 1993), resulting in Taylor-Görtler vortices. In the present case of a detonation wave propagating in channel, the flow is dominated by the strong leading shock wave and following expansion

wave. The pressure and velocity induced by the detonation are quite large compared to the ambient values and hopefully, relatively crude approximations suffice to get estimates of the pressure field that are useful for engineering analysis. Ultimately, the value and validity of such approximations will rest on careful comparison with experimental data.

In order to be useful for simple estimates of the force, it is desirable to have a functional form for f that can be explicity integrated. The following simple form satisfies all the constraints discussed above

$$f = 1 + a \sin(2\theta) \cos\phi \tag{59}$$

where a is a free parameter that we will choose to match the force obtained from independent computation or measurement. A positive value of a implies that pressure on the extrados ($-\pi/2\phi < \pi/2$) is larger than on the intrados ($\pi/2 < \phi < 3\pi/2$). This yields a force that agrees with our previous control analysis of momentum conservation and is consistent with the low-speed flow measurements of pressure distribution (see the data of Ito in Fig. 6 of Berger et al., 1983). The maximum pressure difference between intrados and extrados in turbulent incompressible flow can be correlated as Blevins (2003)

$$[P_{ex} - P_{in}]_{max} = c_k \frac{1}{2} \rho u^2 \qquad c_k = 4 \frac{R_1}{R_2} \left(\frac{5 \times 10^5}{uD/\nu} \right)^{0.17} \tag{60}$$

where $D = 2R_1$ is the pipe diameter, ν is the kinematic viscosity, and u is the average axial velocity. This correlation will only be appropriate in the very low speed portion of the flow near the end of the expansion wave. Moreover, the pressure difference between the inside and outside of the pipe, P_3 - P_a is expected to dominate the force contribution and (60) is only expected to make a minor difference in the total force. For these reasons, we have not used (60) in our preliminary force estimation. If the measurements become sufficiently refined and this correlation can be extended to compressible flow, then it may be possible to refine our force measurements using this type of correlation.

The integrals (54-55) can be carried out explicitly using (59) to yield the force components

$$F_x = F_y = \Delta P(t) \pi R_1^2 \left[1 + a \frac{2}{3} \frac{R_2}{R_1} \right] \tag{61}$$

The value of a can be obtained by equating this result with the results of (42) and recognizing that $A = \pi R_1^2$

$$a = \frac{3}{2} \frac{R_1}{R_2} \left[\frac{\rho u^2}{\Delta P} \right] \tag{62}$$

where we have dropped the subscripts since for quasi-steady flow the properties are the same at the inlet and exit of bend. The quantity in the square brackets can be computed using

the Taylor-Zeldovich model of the flow behind the detonation. The value of this term varies from approximately unity at the detonation front to zero at the end of the expansion wave. A value of zero for a for the no-flow situation is consistent with the considerations at the beginning of this section and yields a force that agrees with the usual static bend analysis (15). A value of unity at the detonation front for the bracketed term in (62) implies that the peak value of the force will be

$$F_x = F_y \approx 2A\Delta P_{CJ} \ . \tag{63}$$

A more precise value of the numerical coefficient is computed subsequently in Section 5 and equal to 1.84, which is nearly identical to the value found by Gross and Minchello (2007), who integrated the pressure field obtained from a CFD computation to determine the force-time history.

The value of a (and f) will in general depend on time since the flow following the detonation is time dependent. From (62) and the TZ solution given in the next section, we can find

$$a(t) = \frac{3}{2}\frac{R_1}{R_2}\left[\frac{\rho(t)u^2(t)}{\Delta P(t)}\right] \tag{64}$$

Substituting this into the expression for f and simplifying, we can compute the x component of force as

$$F_x = \int\int \left[\Delta P(t) + \rho u^2 \frac{3}{2}\frac{R_1}{R_2}\sin(2\theta)\cos\phi\right] n_x \, dA \tag{65}$$

and a similar expression for the y component. The maximum pressure difference across the bend will occur at the midpoint of the bend $\theta = 45°$ and is equal to

$$[P_{ex} - P_{in}]_{max} = 3\frac{R_1}{R_2}\frac{1}{2}\rho u^2 = c_k'\frac{1}{2}\rho u^2 \tag{66}$$

which can be compared to the correlation (60) of the data for the incompressible case. Both expressions have the same dependence on the geometric factor R_1/R_2 and the dynamic head $\frac{1}{2}\rho u^2$, the only difference is in the value of the numerical coefficient multiplying these factors. The equivalent c_k coefficient for our model pressure distribution is

$$c_k' = 3\frac{R_1}{R_2} \tag{67}$$

as computed from (66). At a Reynolds number $Re = uD/\nu$ of 10^5, the incompressible coefficient (60) will be $c_k = 5.25R_1/R_2$ and at a Reynolds number of 10^6, the value is

$3.55R_1/R_2$. These values indicate that our simple model is reasonable and although not identical to the incompressible flow correlation, will give force values that are reasonable estimates for the incompressible and compressible cases at sufficiently high Reynolds numbers that are typical of detonation flows in plant size piping.

4.5 Summary of pressure variation model

The internal pressure dependence on location within the bend is given by combining (59), (46) and (64) to obtain

$$P(t,\theta,\phi) = P_a + \Delta P(t)\left(1 + \sin(2\theta)\cos\phi\frac{3}{2}\frac{R_1}{R_2}\left[\frac{\rho u^2}{\Delta P}\right]\right) \tag{68}$$

The average pressure ΔP and the factor $\rho u^2/\Delta P$ can be computed as functions of time from the Taylor-Zeldovich solution described in Section 5.

5 Ideal Detonation Flow Field

The ideal one-dimensional, adiabatic flow behind a detonation moving at the CJ speed can be represented analytically (see Browne et al. (2004)) for a perfect gas model. The Taylor-Zeldovich (TZ) solution for pressure, velocity, and density is given by the following functions for a detonation that initiated starting at $t = 0$ at location $x = 0$, the closed end of a constant area tube or channel.

$$P(x,t) = \begin{cases} P_1 & U_{CJ} < x/t < \infty \\ P_3\left(1 - \left(\dfrac{\gamma-1}{\gamma+1}\right)\left[1 - \dfrac{x}{a_3 t}\right]\right)^{\frac{2\gamma}{\gamma-1}} & a_3 < x/t < U_{CJ} \\ P_3 & 0 < x/t < a_3 \end{cases} \tag{69}$$

$$\rho(x,t) = \begin{cases} \rho_1 & U_{CJ} < x/t < \infty \\ \rho_3\left(\dfrac{P(x,t)}{P_3}\right)^{1/\gamma} & a_3 < x/t < U_{CJ} \\ \rho_3 & 0 < x/t < a_3 \end{cases} \tag{70}$$

$$u(x,t) = \begin{cases} 0 & U_{CJ} < x/t < \infty \\ \dfrac{2a_3}{\gamma+1}\left[1 - \dfrac{x}{a_3 t}\right] & a_3 < x/t < U_{CJ} \\ 0 & 0 < x/t < a_3 \end{cases} \tag{71}$$

The state 3 is the plateau state of the stationary gas that located next to the closed end. These functions indicate that the flow at an given location is undisturbed (state 1, $u = 0$) before the detonation arrives, there is a limited duration of flow with variable pressure, density and velocity, followed by a static state with pressure P_3. At a fixed time, the spatial distribution of these properties in shown in Fig. 11.

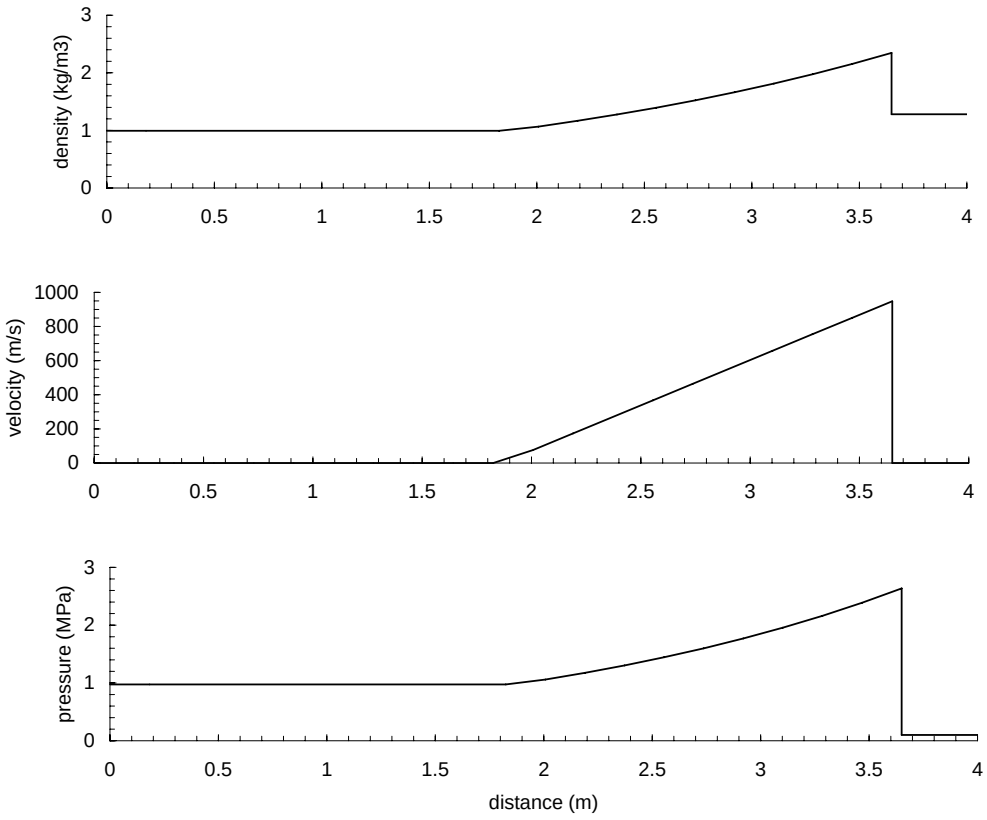

Figure 11: Ideal detonation wave pressure, density and velocity spatial profiles. Numerical values for a H_2-N_2O (30/70) mixture initially at 100 kPa and 295 K. Wave has propagated 3.65 m, corresponding to the distance from igniter the bend in Fig. 3.

5.1 Applying the TZ Model to Bend Entrance and Exit

In order to evaluate the pressure, density, and velocity in the momentum integrals 12, we need to have estimates for these quantities at the entrance (plane 1 in Fig. 7a) and exit (plane 2 in Fig. 7a) of the bend. The model variation of velocity and density within the bend has been previously discussed in Section 4.2.1. The simplest treatment of the propagation inside a bend is to assume that the average flow field is not affected significantly by the bend and that the pressure at the entrance and exit can be obtained from the TZ solution supposing

that the detonation travels on the centerline of the bend at the ideal CJ speed. We can use the data of Fig. 6 obtained in Liang et al. (2008b) to compared directly with the TZ model. The results are shown in Fig. 12 just for the pressure transducers on the bend and with an enlarged time scale that enables the details of the pressure field within the bend to be observed. The TZ model parameters have been chosen to simulate the condition of the tests in the stoichiometric ethylene-oxygen mixtures used in Liang et al. (2008b) and the time origins of the detonation arrival at the bend entrance has been adjusted so that the experimental and model pressure rise coincide at this plane.

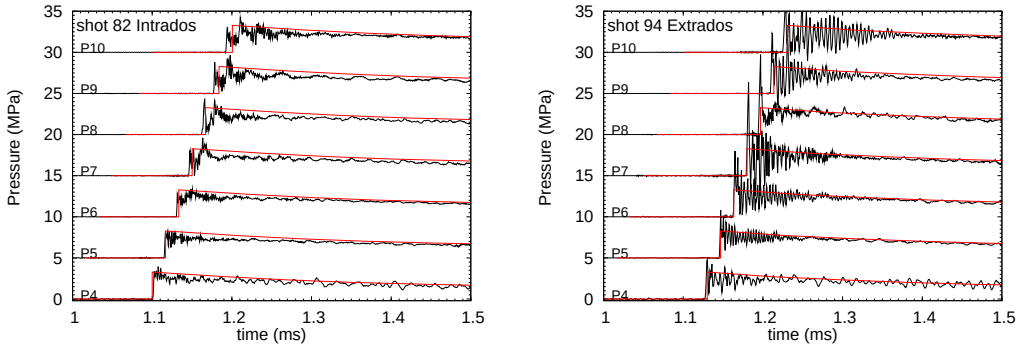

Figure 12: Comparison of pressure measurements with TZ model for detonation propagating through a gradual 90-degree bend in a tube. a) intrados. b) extrados. Liang et al. (2008b)

Note that the high-frequency oscillations observed in Fig. 12b are artifacts of the tube hoop vibration inducing signals on the piezo-electric elements in the pressure transducers. The transducers are compensated for accelerations along the transducer axis but not the accelerations in perpendicular directions. The excitation of these accelerations is much stronger on the extrados than the intrados due to high pressure spike associated with the Mach reflection on the extrados and the difference in mechanical response of the intrados and extrados of the tube. For these reasons only very weak artifacts are observed on the intrados gages.

The comparison shown in Fig. 12 indicate that apart from the first 25 μs, the TZ solution is a reasonable approximation to the mean pressure at the inlet (gage 4 at 0 deg) and exit (gage 10 at 90 deg) planes of the bend. The difference between measured and computed waveforms within the first 252 μs are due to the interaction processes described in Section 3 and Liang et al. (2008b). These variations in the time-history have associated spatial variations across the inlet and exit planes that will contribute to the integrals in the momentum theorem integral approach. We have not measured these and with existing technology, this is not practical. The only possible approach to estimating these terms is high-fidelity computational fluid dynamics, for example, the approach used by Deiterding

(2006, 2007). However, there are substantial difficulties in extending the work of Deiterding (2006) to three-dimensional bends with realistic reaction zones for the very sensitive mixtures of interest to the present application. As a first approximation, we will use the TZ flow field to evaluate the momentum integrals and neglect the temporal and spatial variations that must occur at early times. The validity of this approach will have to be tested against direct experimental measurements of the force, currently in progress in our laboratory.

5.2 Force Estimates based on TZ Model

The momentum theorem model of the bend force (43) can be evaluated using TZ model flow properties. The quantities P, u, and ρ are computed as a function of time and distance from (69- 70) assuming an ignition source located at a specified distance L from a bend of radius R that turns the flow through an angle $\Delta\theta$. We have done this for a H_2-N_2O detonation (30% H_2, 1 atm initial pressure and 25°C initial temperature) using the geometry of the bend in specimen ES-1 with $L = 3.56$, $R = .178$ m, and $\Delta\theta = 90$ deg. This corresponds to the geometry show in Fig. 9 and the experimental situation of initiating the detonation at the west end (left hand side of the figure) and propagating toward the east (right hand side of the figure) end of the specimen. The unsteady and steady portions of the X and Y components of $\vec{F}/A$ are given in Fig. 13. Adding the steady and unsteady portions, the net force in each direction is obtained, see Fig. 14. The effect of the nonsteady contribution is twofold. First, this eliminates the unrealistic jump in force predicted by the quasisteady model and replaces this with a smooth rise during the time the detonation is in the bend. Second, the unsteady force cancels some of steady force in the X direction, reducing the peak amplitude of the force. This is a consequence of the direction of detonation propagation - if the direction of propagation is reversed then the X and Y force time curves would be interchanged. The magnitude of this effect is clearly dependent on extent of unsteadiness which can be measured in terms of the propagation distance L upstream of the bend compared to the radius R of the bend. The forces in each direction have a similar dependence on time with a peak force/area of 3.52 MPa in the X direction and 4.64 MPa in the Y direction. As R/L decreases, both the relative duration of the transient contribution and the difference in force in the X and Y components will decrease. The difference in the X and Y force component magnitudes persists until the flow stops at the end of the Taylor wave, which occurs at about 3.6 ms. As a consequence the net force is initially tilted upward and slowly returns to 45 deg as the flow comes to a stop, see Fig. 15.

The duration of the initial transient associated with the unsteady term is about 0.15 ms, much smaller than the flow duration of about 20 ms that produces the quasi-steady force

that dominates that total impulse. This motivates an approximate model of the force that neglects the initial transient and differences in timing between the X and Y forces. We will evaluate the X and Y contributions at a common location, the midplane of the bend, and drop the unsteady contribution to (43) to obtain the approximate result

$$\vec{F} \approx A\left[P(t) - P_a + \rho(t)u^2(t)\right][\hat{x} + \hat{y}] \tag{72}$$

which has a magnitude of

$$|\vec{F}| \approx A\sqrt{2}\left[P(t) - P_a + \rho(t)u^2(t)\right] \tag{73}$$

This approximation is compared with the result including the transient in Fig. 16. By evaluating the flow quantities in (72) at the midplane of the bend, the peak force magnitude and subsequent time dependence are approximately modeled. The details of the first 0.15 ms are clearly not correctly reproduced and more importantly, the asymmetry of the force is not correctly represented. It would be possible modify this approximation to make it more realistic, for example by including a linear increase in force while the detonation is within the bend and then tilting the force vector toward the Y axis initially and allowing it to relax to 45 deg at the end of the Taylor wave. The success of this type of approximation will depend on the averaging effects of the structural response and relative importance of the unsteady contribution to the force. For the purposes of estimating the peak force and impulse on the bend, we expect that result will be increasingly accurate as the detonation propagation distance upstream of the bend increases relative to the time required for the detonation to propagate through the bend.

Comparing the approximate result with classical low-speed steady-flow result (17), we see that the approximate result is higher than the steady flow by a factor of

$$B = \frac{|\vec{F}|_{(72)}}{|\vec{F}|_{(17)}} = 1 + \frac{\rho u^2}{\Delta P} \tag{74}$$

As shown in Figure 17, the bend force enhancement ratio B varies from about 1.8 at the detonation front to to 1.0 at end of the Taylor wave. The factor $\rho u^2/\Delta P$ was introduced earlier in connection with the internal pressure model (46) to characterize the deviation of the pressure distribution from being spatially uniform due to the high-speed flow behind the detonation front. The magnitude of this parameter can be used as a figure of merit to determine when flow effects are relevant in computing bend forces. For a gas, B is related

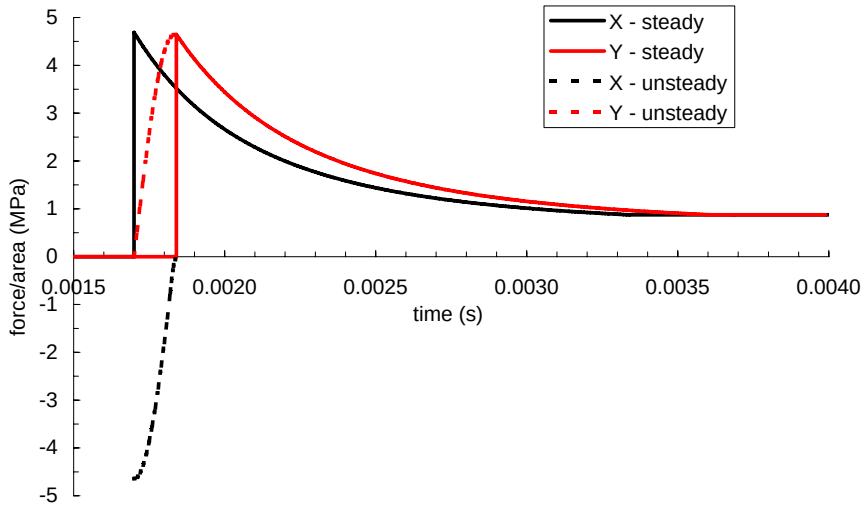

Figure 13: Computation of steady and unsteady components of normalized bend forces F/A using the TZ model to evaluate the momentum integral approach (43) for a detonation propagating through a gradual 90-degree bend in a tube. H_2-N_2O mixture (30/70) at 100 kPa and 295 K.

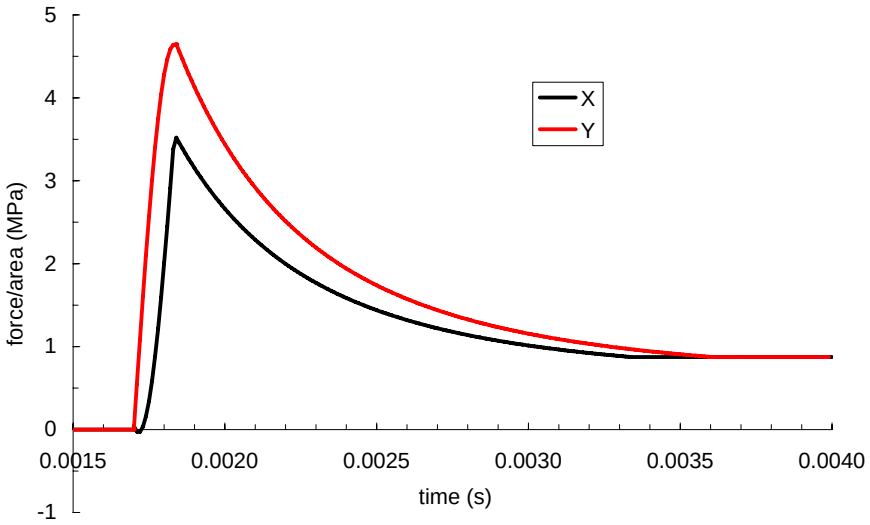

Figure 14: Computation of normalized net bend forces by summing steady and unsteady terms of Fig. 13.

to the Mach number of the flow,

$$M = \frac{u}{a}\,, \tag{75}$$

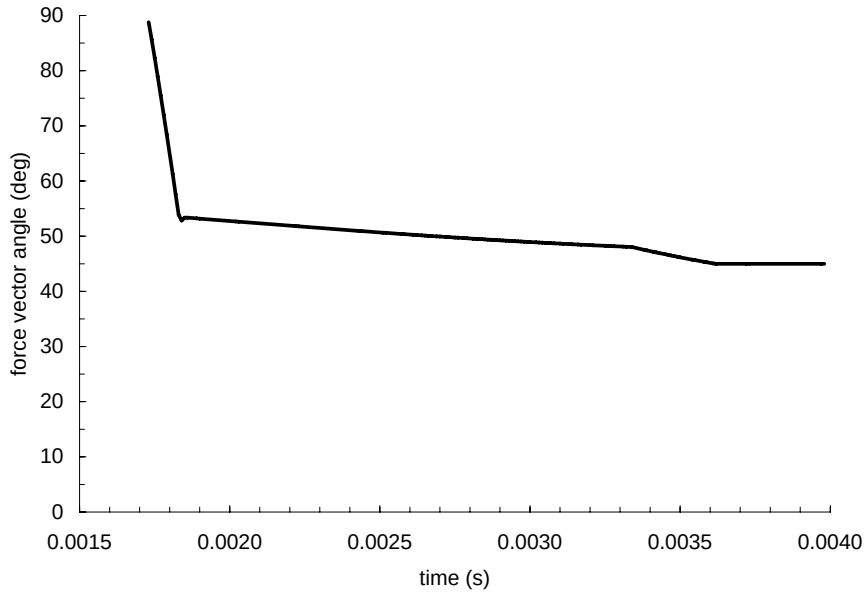

Figure 15: Variation of the direction of force vector, $\tan^{-1}(F_Y/F_x)$, with time for the case shown in Fig. 14.

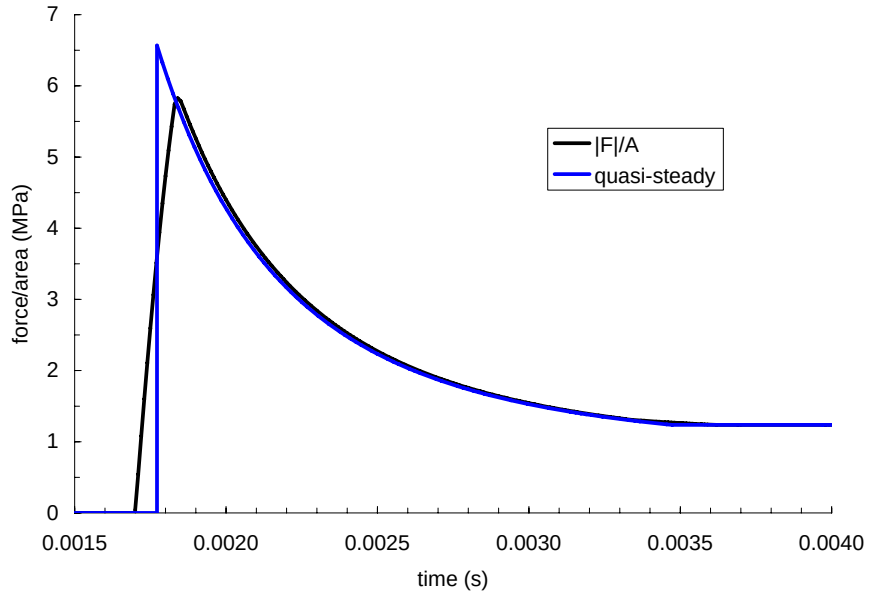

Figure 16: Comparison of the magnitude of the normalized net bend forces $|\vec{F}|/A = \sqrt{F_x^2 + F_y^2}/A$ from Fig. 14 with the quasisteady model (72) evaluated at the midplane of the bend.

where the sound speed a can be computed for an ideal gas as

$$a = \sqrt{\gamma \frac{P}{\rho}} \,. \tag{76}$$

If the pressure is much higher than the ambient pressure (usually the case in detonations), then we can approximate ΔP as P and

$$B \approx 1 + \frac{\rho u^2}{P} \tag{77}$$

$$\approx 1 + \gamma M^2 \tag{78}$$

The value of γ (the ratio of specific heats C_P/C_v) is usually on the order of 1.1 to 1.15 for detonation products so we conclude that we can make a simple estimate of the magnitude for the bend force enhancement as

$$B \sim 1 + 1.15 M^2 \, . \tag{79}$$

The maximum flow Mach number (relative to the pipe) just behind the detonation front is about 0.84, and peak value of $B \sim 1.84$ just behind the wave is consistent with the Mach number and $\gamma \sim 1.155$. Since at a fixed location velocity is decreasing inversely with time (71) following the passage of the wave front, the value of B will decrease to one in the nonlinear fashion as shown in Fig. 17.

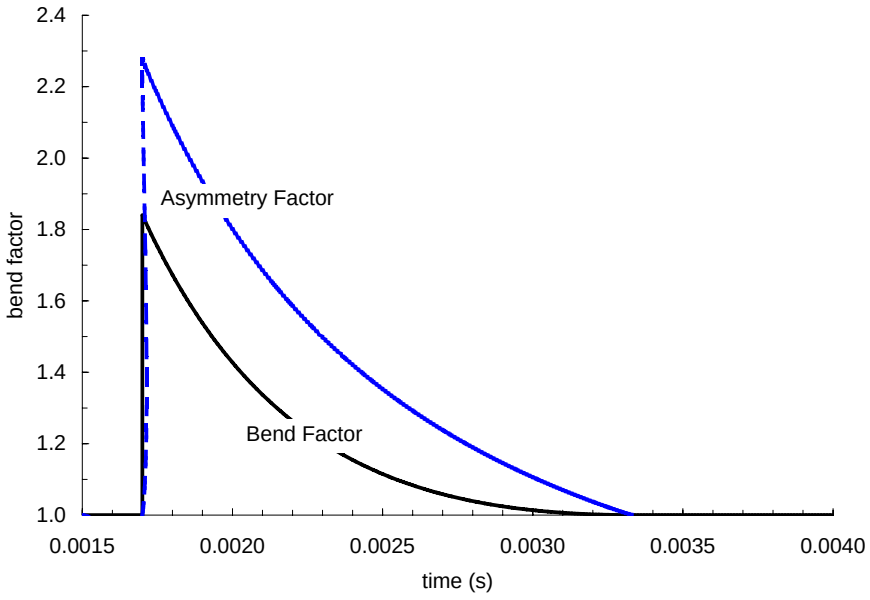

Figure 17: Bend force enhancement factor (74) and Asymmetry factor (80) based on results of Fig. 16 with the quasi-steady model (72) evaluated at the midplane of the bend.

5.2.1 Bend Asymmetry Factor

The factor B is related to the *asymmetry factor* Æ introduced by Gross and Minchello (2007) to account for the observed differences between the FEM computations of bend force and the classical low-speed analysis. In their original formulation, the bend force was computed by assuming that the pressure at the inlet and exit of the bend could be represented as

$$P(t) = Æ\,[P_{tz}(t) - P_3] + P_3 \tag{80}$$

using a constant value of Æ, which was taken to be 2 in the original analysis. This sort of model is intended for application to piping response programs, i.e., ME101, that need point loads as external inputs to simulate the bend forces.

Subsequently, Ahnert (2006c) used in ANSYS simulations a more elaborate version with an angular dependence analogous to that discussed in Section 4.4. The effect of varying the value of Æ, and including time and spatial dependence, was examined by Ligon (2008) with FEM model comparisons to small scale bend tests at CIT in 2006 (Liang et al., 2008b) and ES1 testing in 2008 (Ligon, 2009). Using a value of $Æ = 1.4$ and including an inverse time dependence $Æ = Æ_0(t_{CJ}/t)$ resulted in much better comparison with the measured strains within bend than using the original idea of a constant value of Æ. Comparing (80) with (74), the reasons for this become clear since in order to even approximately match the control volume analysis, Æ must necessarily be time dependent due to the time variation of $B(t)$.

The most recent version of the approximate model (Modified Asymmetry Factor or MAF) is described in Eqs. 3-5 of Ligon (2009) and repeated below.

$$P(t) = Æ\frac{t_o}{t + (t_o - t_a)}\,[P_{tz}(t) - P_3] + P_3 \tag{81}$$

where the arrival time is defined as

$$t_a = \frac{x}{U_{CJ}} \tag{82}$$

and the time parameter t_o has been included to simulate the change in the Taylor wave shape for long propagation distances

$$t_o = t_a \quad \text{for} \quad x < 100D \tag{83}$$

$$t_o = 100\frac{D}{U_{CJ}} \quad \text{for} \quad x > 100D \tag{84}$$

A comparison for the equivalent pressure between the various formulations is shown in Fig. 18 using a value of $\cancel{F} = 2$.

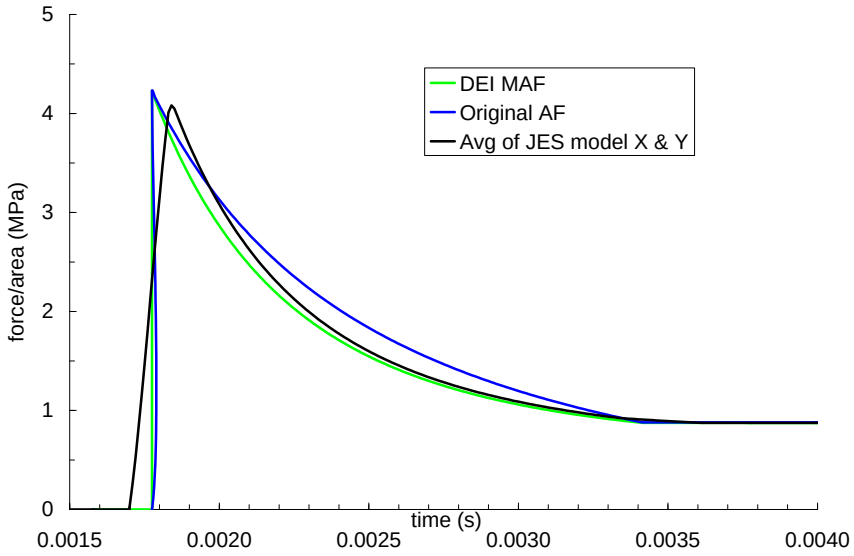

Figure 18: Equivalent pressures for three bend force models.

6 Measuring the Bend Force

The bend force generates axial and transverse (bending) motions in the sections of the piping that extend from the bend. The axial motions are in the form of waves that propagate along the pipe upstream and downstream of the bend and can be detected by axial strain gages mounted on the pipe. The resulting motion of the pipe will also be transmitted to the supports at the ends of the specimen and will create stresses (and associated strains) in the supports. By instrumenting the supports, the deflections and strains can be detected and used to infer the forces generated by the detonation propagating around the bend.

One of the challenges in making measurements of the bend force is to separate the direct effects of the detonation loading (i.e., hoop and axial strain oscillations created immediately after the passage of the detonation) and the waves generated at the bends. This is illustrated in the data from Shot 3 shown in Figure 19. As shown in Fig. 19a, the detonation is initiated at the upper right of the specimen and propagates to the lower left with almost constant speed (within 1% of the CJ velocity of 2088.1 m/s). A reflected shock wave is generated when the detonation reflects from the closed east end of the tube and can be observed propagating in the reverse direction of the initial detonation propagation. In this test, the end flanges of

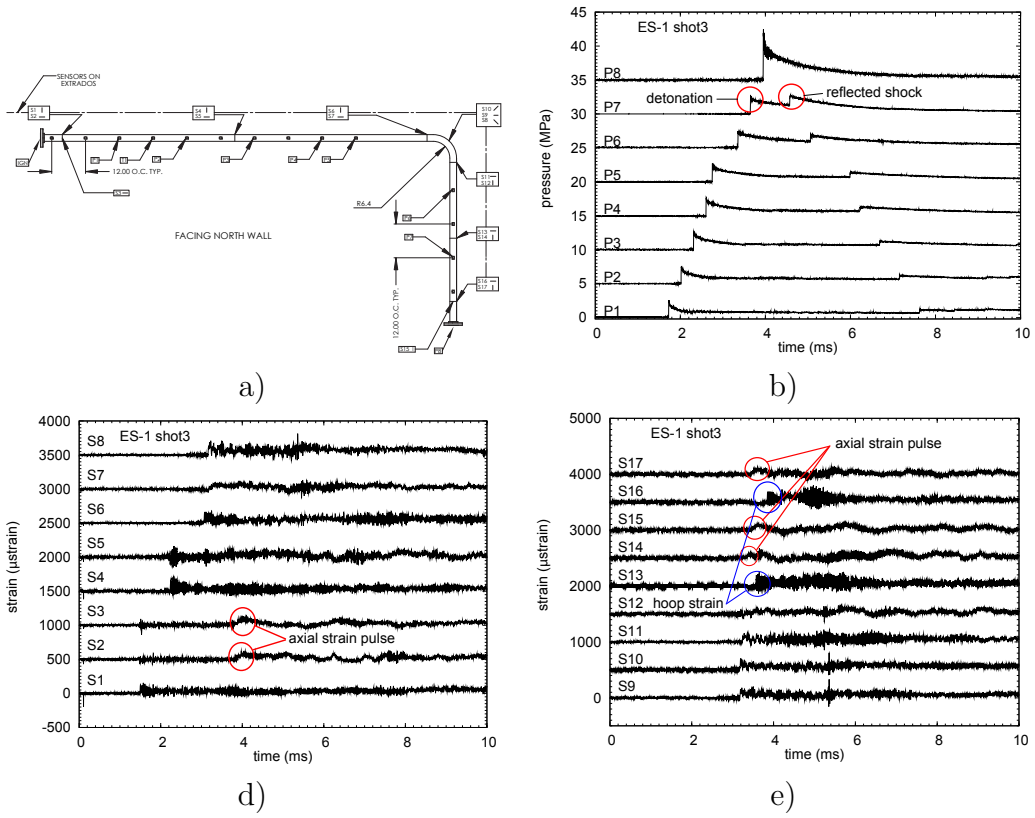

Figure 19: ES1 test 3 setup and data. a) Sensor locations b) Pressure gage data c), d) strain gage data.

the pipe were attached to anchors (see Appendix E) fixed to plates embedded in the walls. The combination of anchors, plates and walls acts effectively as a rigid support to the end of the tube. An alternative arrangement with a cantilever beam support is described in the next section. The strain signal produced when the detonation propagates around the corner can be seen leading the detonation wave on Fig. 19d, signals S14, S15, and S17. The arrival of the detonation at these locations is indicated by the onset of the hoop oscillations in S14 and S16.

On the strain gages downstream from the bend, the axial signal from the bend force leads the signal associated with the pressure transducer since the bend force signal is propagating at approximately the bar speed $\sqrt{E/\rho} = 4900$ m/s and the main axial strain signal associated with the detonation travels at the detonation velocity of 2088 m/s. The distance from the bend to gages S15 and S17 is about 1.4 m so that the leading edge of the strain signal generated by the bend is about 500 μs ahead of the detonation-generated signals. This is about 6 times longer than it takes the detonation to propagate around the bend so that a substantial portion of the bend-generated strain signal is available for analysis.

6.1 Axial strain wave analysis

The force created by the bend is a sudden load that generates axial strain waves that propagate away from the bend location in both directions. A simplified model is to consider the pipe as a bar and the bend force to be applied strictly along the axial direction. This is an approximation that is highly useful since theoretical treatment of axial waves in pipes is quite complex Graff (1991). On the other hand, bar waves are relatively straight forward to model and can be used to relate the applied force to the observed strain. The theory of bar wave propagation Graff (1991) is based on considering the nonsteady force balance for an axial segment of the bar. Balancing forces on each end of a short segment with the inertial forces of acceleration, the governing equation of bar motion is obtained

$$\frac{\partial \sigma}{\partial x} = \frac{\rho}{E}\frac{\partial^2 u}{\partial t^2} \tag{85}$$

where the axial stress σ is related to the strain ϵ by Hooke's law

$$\sigma = E\epsilon \tag{86}$$

and the strain is related to displacement by

$$\epsilon = \frac{\partial u}{\partial x} \, . \tag{87}$$

which is equivalent to the one-dimensional wave equation for waves propagating with the bar speed $c_b = \sqrt{E/\rho}$.

$$\frac{\partial^2 u}{\partial x^2} = \frac{1}{c_b^2}\frac{\partial^2 u}{\partial t^2} \, . \tag{88}$$

The solution is given by d'Alembert's formula

$$u = f(x - c_b t) + g(x + c_b t) \tag{89}$$

where f and g are functions that are determined by the initial and boundary conditions. This form of the solution also applies to stresses as well as strains.

If a force $F(t)$ is applied at the bend, then the stress will be $\sigma(t) = F(t)/A_p$. By

d'Alembert's solution the stress at a distance x and time t will be

$$\sigma(x,t) = \frac{1}{A_p} F(x - c_b t) \tag{90}$$

where A_p is the cross-sectional area of the pipe metal. By Hooke's Law, the strain is

$$\epsilon(x,t) = \frac{1}{EA_p} F(x - c_b t) \tag{91}$$

Using the force model based on the control volume model, the predicted strains are given in Fig. 20. Comparison with the data of Test 3 for the axial strain gages S2 and S3, which are

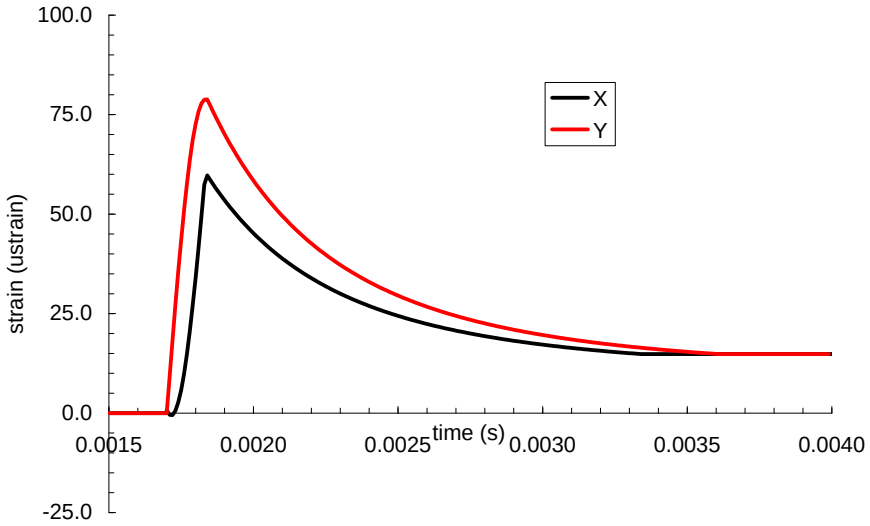

Figure 20: Axial strains predicted by the control volume force and bar wave propagation models.

located upstream (W end) of the bend, and the axial strain gages S15 and S17, which are located downstream (E end) of the bend is shown in Fig. 21. The predicted and observed downstream strain history (Fig. 21b) are in good agreement for the first 300–400 μs, which is the time available for observation before the detonation arrives at this location. In particular, the observed peak value of the strain is 90 μstrain, and the predicted value is 78 μstrain. The observed peak strain corresponds to a peak force of 12 kN (2700 lb), about 15% higher than the predicted peak corner force of 10.4 kN (2340 lb).

The disagreement at later times is due to both the axial strain signal induced by the detonation passing these locations and more importantly, the reflection of the axial strain wave from the end flange and anchor support structure. The reflection process will result in a series of reflected compression and tension waves that arise from the three-dimensional

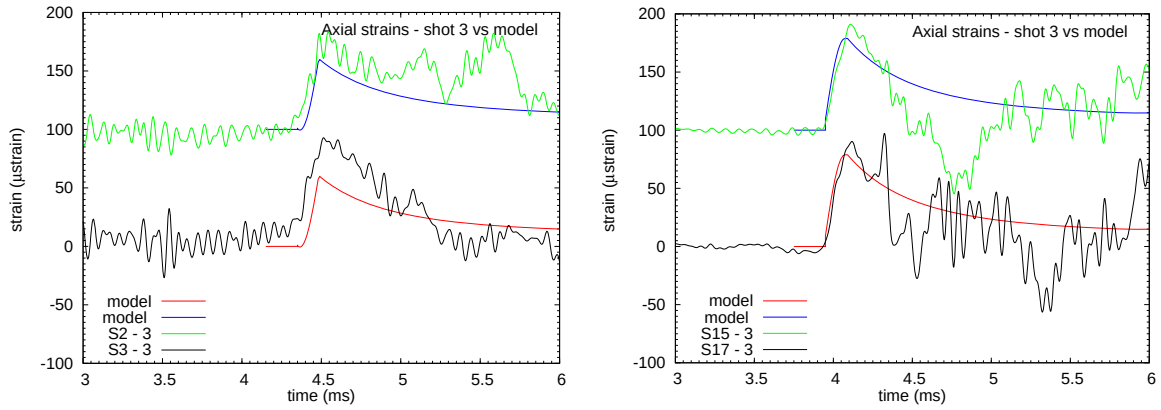

a b

Figure 21: Axial strains predicted by the control volume force model compared to measured strains in test 3. a) upstream of bend b) downstream of bend.

elastic wave propagation in the support structure. There are no simple models for this process but finite element simulations of this interaction are able to capture the most of the details by modeling the flange and anchor support as rigid boundary.

The comparison of the predicted and observed upstream strain history (Fig. 21a) is complicated by the presence of significant axial strain oscillations created by Poisson coupling to the 29 kHz hoop oscillations created by the detonation passage several ms earlier. The amplitude of these oscillations is as large as 40 μstrain prior to the arrival of axial strain waves from the bend. Without correcting for these oscillations, we observe peak strains that are on the order of 90 μstrain - similar to the downstream peak values - and the control volume model predicts peak strains on the order of 60 μstrain. Ignoring the oscillations, the overall time history appears to have the qualitatively correct shape for the first 500 μs, after which the reflected strain pulse creates significant differences between measured and model strain histories.

6.2 Force Link Analysis

A cantilever beam was attached to the vertical leg of the bend specimen ES1 and instrumented with strain gages as described in Appendix C. In order to compute the actual force from the deflection of the beam, the system dynamics must be accounted for. This includes flexural waves on the beam as well as the inertia of the piping components tied to the force link. If we suppose that the motions are sufficiently low in frequency compared to the natural frequencies of the beam ($\geq$ 818 Hz), then we can approximate the dynamics of the beam bending as a simple spring and treat the problem as a single degree of freedom system. The

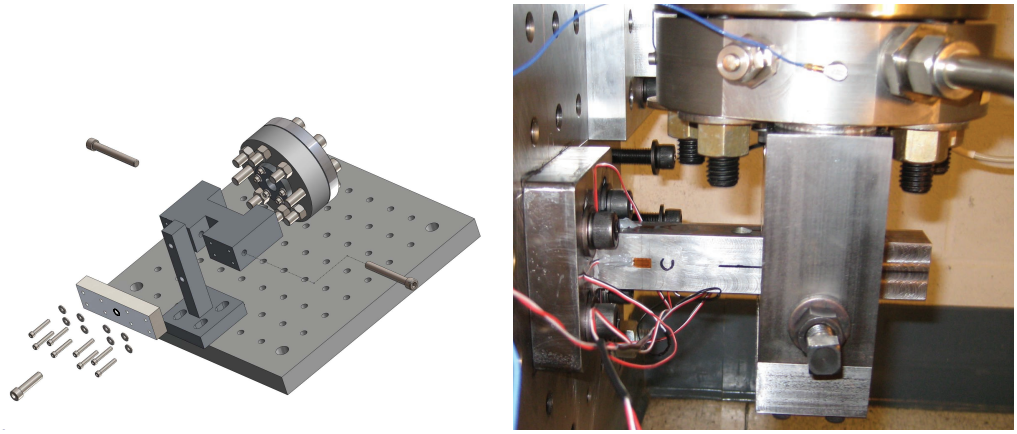

a b

Figure 22: Force link and cantilever beam used to to measure forces at lower east end of ES1. a) exploded view b) side view showing strain gages.

dynamics are determined by Newton's law of motion which can be written in terms of the downward deflection Y of the cantilever at the point of force application.

$$M\frac{d^2Y}{dt^2} + k_y Y = F(t) \tag{92}$$

where the applied load F is due to both the axial strain waves in the pipe and the pressure in the gas created by the detonation reflection.

$$F(t) = A_p\sigma_x(t) + A_i[P(t) - P_0] \tag{93}$$

Consider the situation of a cantilever beam mounted at the east end of ES1 with deflections primarily in the vertical direction. Initially the pipe specimen and the cantilever are at rest and a detonation is initiated at the west end of the pipe, propagates toward the east, around the bend and then reflects from the bottom of the east end as a shock wave. The forcing due to the tube stress is zero until the bar wave generated by the bend force arrives at the east end of the pipe. The bar wave travels at approximately 5000 m/s and the detonation at 2100 m/s, so that the bar wave arrives at the east end of the tube about 50 μs ahead of the detonation.

The bar wave is a propagating axial tension wave which will be transmitted into the force link as an upward force and reflected as an axial tension wave propagating upward toward the bend. Because the mass of the flange and force link is relatively large and slow to move, the east end of the pipe will act effectively as a fixed (rigid) boundary so that

the tension in the pipe will approximately double upon reflection of the bar stress wave (See p. 80 ff of Graff, 1991). The upward force on the cantilever will suddenly increase when the bar wave arrives, accelerating the mass and beam upward and placing the upper fibers of the beam in compression. The pressure forcing term is zero until the detonation wave arrives at the end of the tube and reversing the direction of the applied force. The upward motion of the cantilever will slow and eventually reverse, placing the upper fibers of the beam in tension. These two forces excite the oscillation of the spring-mass system and give rise to the initial potion of the oscillatory strain signal observed by the cantilever strain gages. The dynamics of the cantilever and end flange mass are coupled to the motion

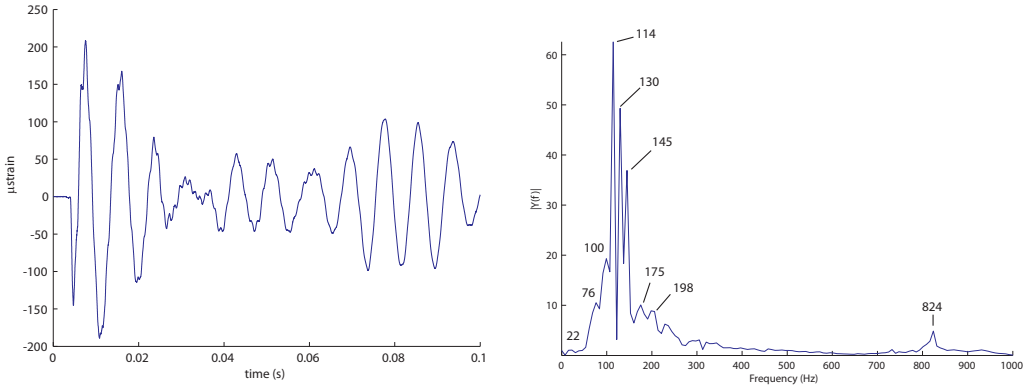

a b

Figure 23: Bending strain on cantilever beam at lower east end of ES1, shot 33. a) History of bending strain in the vertical direction from gage pair S24 b) frequency spectrum.

of the piping system which is set into motion due to the excitation of vibrations by the forcing created from detonation propagation around the bend. There are a large number of vibrational modes possible but the lowest-order modes that appear most likely to be excited are primarily in-plane beam bending of the horizontal and vertical segments of the specimen, see the results of FEM vibrational analysis shown in Appendix D. The pipe specimen ends and the elbow are relatively rigid so that the ends of these segments are approximately nodal points of minimum deflection. The rotation and deflection of the bend will couple the vibrations of the vertical to horizontal segments of the piping specimen. These vibrations will result in axial strains on the cantilever-flange system, forcing the motion at the characteristic frequency of the piping vibration. Due the coupling between the vibrations of the cantilever and the vibrational modes of the piping system, the resulting oscillation of the cantilever is not a single frequency. The spectral analysis of the strain history S24 shown in Fig. 23b shows at least 10 distinct modes between 20 and 1000 Hz. The majority of the energy is in modes between 100 and 150 Hz, which corresponds to computed modes 8, 9 and 10 of Model

5 in Appendix D.

This means that at a minimum the SDOF model parameters for the free beam obtained in Appendix C cannot be directly applied to case of a cantilever attached to the pipe. In general, the piping system also has a number of degrees of freedom in addition to just vertical motion, and the loading is distributed along the piping system. If we wish to account for all of this complexity in reconstructing forces from measured strains, then some version of the sensitivity response method (described in Chap. 5 of Doyle, 2004) must be applied. This requires either very high-fidelity FEM model of the entire system or careful analysis of the experimental response function as discussed by Martin and Doyle (1996), Doyle (1997b). However, an idea of the issues involved can be obtained by ignoring wave propagation in the piping system and analyzing the coupled motion as a single-degree-of-freedom spring-mass system as discussed below.

The beams are coupled to the piping system which has both stiffness and inertia. For vertical motions of the vertical leg of the piping, the horizontal leg resists vertical motion by bending. If the length of the horizontal leg is H, then the stiffness can be computed by treating the pipe as an annular beam with a moment of inertia

$$I_z = \frac{\pi}{4}\left(D_o^4 - D_i^4\right) \tag{94}$$

$$= 4.341 \times 10^{-6} \quad \text{m}^4 \tag{95}$$

and beam length $H = 3.6$ m. From the standard beam expressions, the stiffness is

$$k_H = \frac{3EI}{H^3} \tag{96}$$

$$= 5.58 \times 10^4 \quad \text{N/m} \tag{97}$$

which is a factor of 500 less stiff than the cantilever beam, suggesting that we can neglect the stiffness of the horizontal leg of the piping in comparison with the cantilever beam support. The mass of the piping system is about 5.44 kg/m and vertical leg of ES1 is 1.7 m high so that the mass of the vertical leg is approximately 9.14 kg. The bottom flange assembly and the force link together have a mass of 17.6 kg. The total mass of the components on the vertical leg of the piping system is approximately 26.7 kg. Some fraction of the horizontal piping system mass of 20 kg may also participate in the vertical motion. A rough estimate of this mass can be made by lumping the vibrations observed between 100 and 150 Hz into a single mode at 125 Hz and back-calculating the mass using the SDOF model and known stiffness of the cantilever. The resulting value is 46 Kg, which is fortuitously close to the

total mass of piping, flanges, and cantilever beam fixture at the lower end of ES1.

The resonant frequency of the spring-mass system consisting of the cantilever, flanges, and vertical piping is approximately

$$f = \frac{1}{2\pi}\sqrt{\frac{k_y}{M}} \tag{98}$$

where we have neglected both the mass of the beam and the stiffness of the horizontal piping leg. Subsituting the values for the mass (26.7 kg) and spring constant (2.851 $\times 10^7$ N/m) of the cantilever, we find that

$$f = 165 \quad \text{Hz} \tag{99}$$

A peak at 175 Hz is visible in Fig. 23 that may correspond to this oscillation mode. The mode at 198 Hz may correspond to the computed 202 Hz oscillation with only the 17.6 kg mass of flange components participating.

Contrast these frequencies with the lowest natural bending frequency of the cantilever beam alone (Table 8.1, Case 3 of Blevins, 1979).

$$f_{beam} = \frac{\lambda_i^2}{2\pi L^2}\sqrt{\frac{EI}{m}} \tag{100}$$

where $m = \rho bh$ is the mass/length of the beam and $\lambda_1 = 1.875$. Substituting the values for the ES1 cantilevers, we obtain

$$f_{beam} = 818 \quad \text{Hz} \tag{101}$$

A value close to this (824 Hz) can be observed as a small peak in the spectrum of S24 shown in Fig. 23. Note for the natural frequency computation, the entire length of the cantilever (7 in) is used whereas for the spring constant computation, only the distance from the root to the application of the load (4.5 in) is used. The section of the cantilever from 4.5 to 7 in is essentially stress free (except for a small region near the loaded section) in the force measurement application. Since this portion does not bend, it does not play a role in determining the spring constant.

Using the SDOF model and interpreting the measured strains of the cantilever in terms of deflections with the static beam expressions, we can back calculate the forces on the cantilever by treating the beam response as quasi-static and computing the dynamics of the beam-piping system as a single degree of freedom model (92). From static beam theory and

using the notation in Appendix C, the deflection-strain relation is

$$Y' = \frac{2x_p^3}{3h(x_{sg} - x_p)}\epsilon \tag{102}$$

$$\alpha\epsilon \ , \tag{103}$$

$$\alpha = 3.532 \times 10^{-7} \quad \mathrm{m}/\mu\mathrm{strain} \ . \tag{104}$$

In order to carry out the evaluation of the left-hand side of (92), we need to evaluate the second derivative of the strain history. To do this, we have used the Savitzky-Golay method (MathWorks) of least-squares fitting of a local polynomial to provide smoothed data and derivatives at each data point. We used segments 311 points long and fit 3rd order polynomials to carry this out on the original data. The effective mass and stiffness were chosen to be 26 kg and 2.851 $\times 10^7$ N/m, consistent with the physical model discussed above. The resulting force (Fig. 24) is dominated by the acceleration effects. The peak values of the forces associated with acceleration are 12 kN, which are 6 times larger than the peak forces of 2 kN associated with quasi-static deflection.

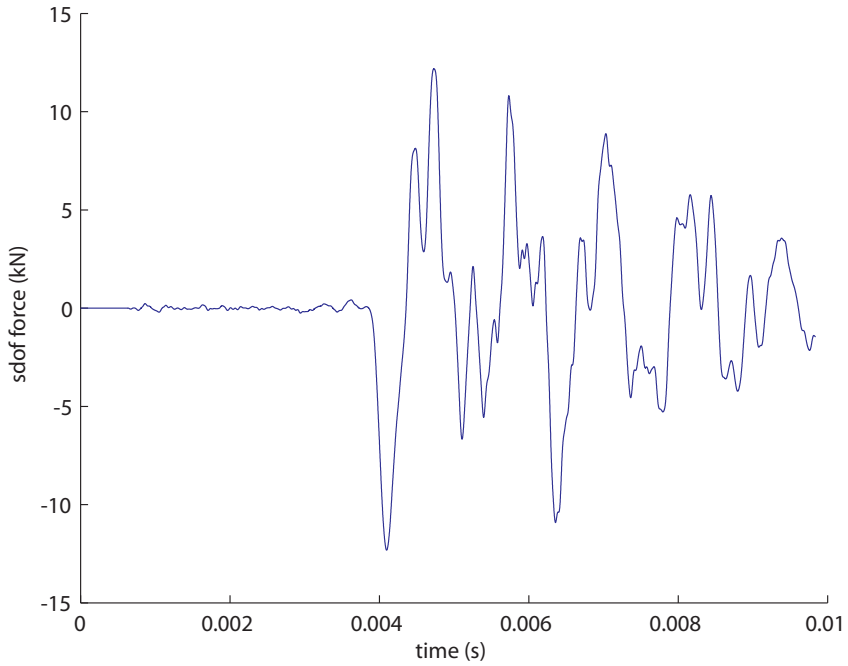

Figure 24: Force on cantilever beam at lower east end of ES1, shot 33. Results obtained from SDOF model and measured strain history for bending in the vertical direction.

The derived force is consistent with pressure and strain histories shown in Fig. 19. The initial upward deflection of the beam is created by the arrival of the bend-force tension pulse

running ahead of the detonation. The initial peak value of the force, -12.15 kN is obtained at a time of 4.108 ms, which is 0.2 ms after the arrival of the pressure wave at the gage P8. The peak value is consistent with the measured value of the strain at gages S15 and S17 as well as the estimates from the bend force control volume model. The force reverses direction and reaches a peak value of +12.2 kN at 4.732 ms, consistent with the peak reflected detonation pressure of 6.5 MPa which implies a peak force of 13.6 kN. The peak values of the force and the details of the force-time history depend on the amount of smoothing (length of data segments and order of the polynomial). We selected the smoothing parameters based on the visual appearance of the computed second derivative. Shorter data segments or higher order polynomials resulted in much noisier signals although some of this noise is actually high-frequency vibrations of the piping system. The choice of smoothing parameters we are using corresponds to filtering out all noise and vibrations above 3 kHz.

One of the issues in interpreting the force link data that we have not addressed is the out-of-plane motion. As shown in Fig. 25 is that there is a significant amount of cantilever bending in the horizontal direction, which is a consequence of the horizontal deflection and rotation about the vertical axis of the pipe as shown in modes 8, 9, 10 and 11 in Appendix D. Our analysis of vertical motion does not include any of these effects. At best, the SDOF model in the vertical direction will only be approximately correct up to about 6 ms and is clearly incorrect after that. Both the horizontal and rotational motions of the coupled piping-support system will have to be included in order to correctly describe the true forces on the lower end of the piping system.

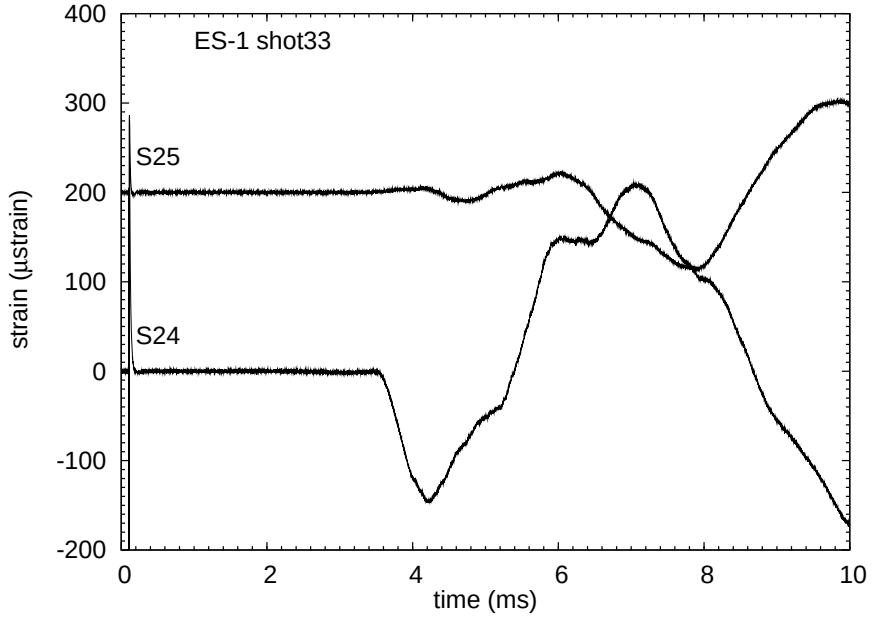

Figure 25: Strain history on cantilever beam at lower east end of ES1, shot 33. S24 measures bending in the vertical (in plane) direction, S25 measures the bending in the horizontal (out of plane) direction.

7 Summary

We have developed analytical approaches to the computation of forces due to a gaseous detonation propagating through a rigid piping bend. The force calculations are based on the integral version of the momentum conservation theorem, the appropriate choice of a control volume, and approximation of the flow field behind the detonation wave using the Taylor-Zeldovich model extended to curved pipes. We have measured axial strains and forces on support beams. Using simple models of wave propagation in the piping and SDOF models for the beam-piping vertical motion, we have interpreted strains in terms of forces and compared the results with the force models.

The analysis and models are designed to provide a theoretical basis for an empirical model of bend forces that was developed by Gross and Minchello (2007). Our analysis explains the origin of the "asymmetry factor" as due to the contribution of gas motion to the momentum flux in the high speed flow behind the detonation wave. There is an additional contribution at early times due to the unsteady or storage effect of the detonation wave filling the initially empty bend segment of piping. We show that the pressure distribution inside the bend must be spatial nonuniform in order to be consistent with the momentum theorem. A simple model for the spatially nonuniformity is proposed and determines the functional dependence so that both the average internal pressure and net force are consistent with experimental observations and the integral analysis.

Two approximate models are given that are specifically intended for use in vibration modeling of piping systems.

External Force Model This model is presented in Section 4.3 and gives an estimate of the force $\vec{F}(t)$ as a function of time. This estimate is useful as an externally applied load for structural frame model of a piping system as represented in structural dynamics simulation such as Bechtel's ME101 computer code. A simplified version of this model (9) concentrates the load at a single location at the midplane of the bend and in the direction bisecting the bend. The equations have been developed for the case of a 90° bend but can be readily extended to bends through an arbitrary angle. The model is independent of the radius of the bend or diameter of the pipe but does assume that the bend is relatively gentle and that the extend of the bend is small compared to the detonation propagation distance upstream of the bend.

Internal Pressure Model This model is presented in Section 4.4 and give an estimate of the internal pressure within the pipe bend as a function of time and position. This estimate is useful as an internally applied traveling load used with a finite element simulation such as

ANSYS. A model spatial distribution function was proposed and it contained one adjustable parameter which was selected so that when the pressure distribution was integrated over the bend, the total force matched the value predicted by the integral method. The equations were developed for a 90° bend but can be extended to work for arbitrary angles.

Bend Factor The ratio $\rho u^2/\Delta P$ plays an important role in determining the deviation of the results from the classic formulas for low-speed flow. For low-speed flow in gases, this factor is close to zero and the standard methods of bend force estimation using static pressure (15) are applicable. In high-speed gas flow, this term is almost 1 behind the detonation and decreases to zero as the flow decreases to zero in the Taylor wave (Fig. 11). In the simplest version of the bend force model (72) for detonation waves, the classical result can be corrected by using a time-dependent (Fig. 15) bend factor

$$B = 1 + \rho u^2/\Delta P \tag{105}$$

multiplier on the low-speed result to compute the forces

$$\vec{F} \approx A\Delta P(t)B(t)\,[\hat{x} + \hat{y}] \tag{106}$$

with the pressure difference ΔP evaluated using the TZ solution (69)-(71) to the flow.

Force Measurement The axial stress waves and cantilever beam reaction forces can be both be used to estimate the peak value of the forces created by the detonation propagating around the bend. Both techniques give an experimental value of 12 ± 1 kN for the bend peak force generated in the downstream leg of the piping system. The force is directed axially and of similar magnitude to the peak force developed by detonation reflection.

8 Acknowledgement

This work was funded by the Project Assistance Corporation and carried out in support of the US Department of Energy, Office of River Protection program on Hydrogen in Piping and Ancillary Vessels (HPAV) for the Waste Treatment Plant at Hanford, WA. The program manager at the DOE is Greg Jones. We thank Jason Damazo for checking the algebra for the bend force control model and carrying out the SW simulations of ES1 vibrational modes. David Gross and Tom Ligon of DEI carried out the companion FEM study of ES1 data, developed an improved bend force model, and contributed substantially to our understanding

of the piping system response.

References

S. Ahnert. Detonation response of ASX sampler piping system. DEI Calculation No. C-6908-00-19, September 2006a. 11, 23

S. Ahnert. DDT pulse shape elastic validation. DEI Calculation No. C-6908-00-27, June 2006b. 10

S. D. Ahnert. System response benchmark validation. Calculation Note C-6908-00-26, Dominion Engineering, Inc., August 2006c. Issued as Bechtel Supplier Document 24590-QL-HC4-W000-0067. 11, 43

George A. Antaki. *Piping and Pipeline Engineering*. CRC Press, 2003. 10

ASME. *Power Piping: ASME Code for Pressure Piping, B31*. American Society of Mechanical Engineers, 2001. ANSI standard ASME B31.1-2001. 10

W.M. Beltman and J.E. Shepherd. Linear elastic response of tubes to internal detonation loading. *Journal of Sound and Vibration*, 252(4):617–655, 2002. 10, 12

S. A. Berger, L. Talbot, and L.-S. Yao. Flow in curved pipes. *Ann. Rev. Fluid Mech.*, 15: 461–512, 1983. 32, 33

R. D. Blevins. *Formulas for natural frequency and mode shape*. van Nostrand Reinhold Company, 1979. 12, 13, 52

R. D. Blevins. *Vibration of Structures Induced by Flow*, chapter 29. In Harris and Piersol (2002), fifth edition, 2002. 29

R. D. Blevins. *Applied Fluid Dynamics Handbook*. Krieger, 2003. 33

A. Bray, G. Barbato, and R. Levi. *Theory and practice of Force Measurement*. Academic Press, 1990. 66

S. Browne, J. Ziegler, and J. E. Shepherd. Numerical solution methods for shock and detonation jump conditions. Technical Report FM2006.006, GALCIT, 2004. 8, 35, 64

Ralf Deiterding. Dynamically adaptive simulation of regular detonation structures using the cartesian mesh refinement framework AMROC. *Int. J. Computational Science and Engineering*, 1(1/2/3):64–74, 2006. 5, 18, 37, 38

Ralf Deiterding. Numerical simulation of transient detonation structures in h2-o2 mixtures in smooth pipe bends. In Proc. of the 21st International Colloquium on the Dynamics of Explosions and Reactive Systems, Poitiers, Jul, 2007, July 2007. 18, 38

J. F. Doyle. *Wave Propagation in Structures*. Springer, 2nd edition, 1997a. 73

J. F. Doyle. A wavelet deconvolution method for impact force identification. *Experimental Mechanics*, 37(4):403–408, 1997b. 51

J. F. Doyle. *Modern Experimental Stress Analysis*. Wiley, 2004. 51, 71

D. H. Edwards, P. Fearnley, and M. A. Nettleton. Shock diffraction in channels with 90° bends. *J. Fluid Mech.*, 132:257–270, 1983. 17

Karl F. Graff. *Wave Motion in Elastic Solids*. Dover, 1991. 46, 50

D. J. Gross and J. C. Minchello. DOE questions regarding HPAV inputs to piping system response models. DEI Memo M-6908-00-36, April 2007. 23, 34, 43, 56

C. M. Harris and A. G. Piersol, editors. *Harris' Shock and Vibration Handbook*. McGraw-Hill, fifth edition, 2002. 59

W. D. Henshaw, N.F. Smyth, and D. W. Schwendeman. Numerical shock propagation using geometrical shock dynamics. *J. Fluid Mech.*, 171:517–545, 1986. 17

Z. Liang, J. Karnesky, and J.E. Shepherd. Structural response to reflected detonations and deflagration-to-detonation transition in H_2-N_2O mixtures. Technical Report FM2006-003, Graduate Aeronautical Laboratory, California Institute of Technology, August 2006. 10

Z. Liang, T. Curran, and J. E. Shepherd. Structural response to detonation loading in a 90-degree bend. In Klaus Hannemann and Friedrich Seiler, editors, *Proceedings of the 26th International Symposium on Shock Waves*. Springer, 2008a. In press, presented at 26th ISSW Gttingen, Germany, 15-20 July 2007. 5, 19

Z. Liang, T. Curran, and J. E. Shepherd. Structural response of piping components to detonation loading. Technical Report FM2006.008, Graduate Aeronautical Laboratories, California Institute of Technology, August 2008b. 5, 19, 37, 43

T. Ligon. Pipe bend asymmetry factor response validation. DEI Calculation No. C-6908-00-38, February 2008. 24, 43

T. Ligon. The idealized PRC-DDT pulse shape validation. DEI Calculation No. C-6916-00-04, In revision, March 2010, February 2009. 43

M. T. Martin and J. F. Doyle. Impact force identification from wave propagation responses. *Int. J. Impact Engng*, 18(1):65–77, 1996. 51

The MathWorks. MatLab: The language of technical computing. version 7.3.0.267 (R2006b). See documentation on `sgolay` function at `http://www.mathworks.com`. 53, 71

Kenneth G. McConnell. *Vibration Testing: Theory and Practice*. Wiley, 1995. 71

F. J. Moody. *Introduction to Unsteady Thermofluid Dynamics*. J. Wiley and Sons, 1990. 21

David E. Olson. *Pipe Vibration Testing and Analysis*, chapter 37. Volume 2 of Rao (2002), 2002. 11, 22

M.D. Olson. Efficient modelling of blast loaded stiffened plate and cylindrical shell structures. *Computers and structures*, 40(5):1139–1149, 1991. 23

C. C. Perry. Measurement of force, torque, and other mechanical variables with strain gages. Measurements Group technical note downloaded November 2008 from `http://www.davidson.com.au/products/strain/mg/technology/technotes.asp`, 2008. 66

K. R. Rao, editor. *Companion Guide to the ASME Boiler and Pressure Vessel Code*, volume 2. ASME Press, 2002. 10, 61

K. R. Rao, editor. *Companion Guide to the ASME Boiler and Pressure Vessel Code*, volume 1. ASME Press, second edition, 2006. 10

Everett C. Rodabaugh. *Stress Intensification Factors, Stress Indices, and Fexibility Factors*, chapter 38. Volume 2 of Rao (2002), 2002. 10, 20

J. E. Shepherd. Structural response of piping to internal gas detonation. *Journal of Pressure Vessel Technology*, 131(3), 2009. 9

J. E. Shepherd, J. Karnesky, F. Pintgen, and J. C. Krok. Experimental measurements of strains and blast waves resulting from detonations in tubes. Technical Report FM2006.010, Graduate Aeronautical Laboratories, California Institute of Technology, 2008. 10, 12

J.E. Shepherd and R. Akbar. Piping system response to detonations. Technical Report FM2009-001, Graduate Aeronautical Laboratories California Institute of Technology, May 2010. 9

J.E. Shepherd, E. Schultz, and R. Akbar. Detonation diffraction. In G. Ball, R. Hillier, and G. Roberts, editors, *Proceedings of the 22nd International Symposium on Shock Waves*, volume 1, pages 41–48, 2000. 18

G.O. Thomas. The response of pipes and supports generated by gaseous detonations. *Journal of Pressure Vessel Technology*, 124:66–73, 2002. 11, 19

A.C. Ugural and S.K. Fenster. *Advanced Strength and Applied Elasticity*. Elsevier, 2nd si edition, 1987. 65

J. P. Vanyo. *Rotating Fluids in Engineering and Science*. Dover, 1993. 32

R. L. Williams and G. O. Thomas. Detonation interaction with wedges and bends. *Shock Waves*, 11:481–492, 2002. 17, 19

A Properties of Schedule 40 pipe

Table 2: 2-in Schedule 40 Stainless Steel pipe, nominal properties.

Outer diameter	2.375	in	60.3	mm
Inner diameter	2.067	in	52.5	mm
Mean radius R	2.22	in	0.0282067	m
Pipe metal cross-sectional area A_p	1.075	in^2	6.910×10^{-4}	m^2
Flow cross-sectional area A_i	3.356	in^2	2.165×10^{-3}	m^2
Young's modulus E	2.79×10^6	psi	1.93×10^{11}	Pa
mass density ρ	0.29	lb/in^3	8040	kg/m^3
Poisson ratio ν	0.305			
Specific heat capacity C_p			500	J/kg-K
Thermal expansion coefficient (linear) α			16.9 × 10−6	K^{-1}
Thermal conductivity k			16.2	W/m-K
thickness h	0.154	in	0.0039116	m
hoop frequency f_{hoop}	29.0	kHz		

B Properties of CJ wave in H_2-N_2O

Table 3: Properties of CJ detonation in standard (0.3/0.7) H_2-N_2O mixture as computed with the Shock and Detonation Toolbox Browne et al. (2004).

```
   Pressure 100000 (Pa)
   Temperature 295 (K)
   Density 1.2807 (kg/m3)
   a1 (frozen) 319.2198 (m/s)
   gamma1 (frozen) 1.3051 (m/s)
Computing CJ state and isentrope for H2:0.3 N2O:0.7 using H2-N2O.cti
CJ speed 2088.0993 (m/s)
CJ State
   Pressure 2631195.6132 (Pa)
   Temperature 3382.936 (K)
   Density 2.3426 (kg/m3)
   Entropy 10352.4577 (J/kg-K)
   w2 (wave frame) 1141.6216 (m/s)
   u2 (lab frame) 946.4776 (m/s)
   a2 (frozen) 1186.9148 (m/s)
   a2 (equilibrium) 1139.7912 (m/s)
   Gamma2 (frozen) 1.2542 (m/s)
   Gamma2 (equilibrium) 1.1566 (m/s)
Detonation CJ Mach number) 6.5413 (m/s)
2-gamma energy parameter q 6432443.2096 (J/kg)
Generating points on isentrope and computing Taylor wave velocity
State 3
   Pressure 958322.0076 (Pa)
   Temperature 3004.943 (K)
   Volume 1.0218 (m3/kg)
   Sound speed (frozen) 1107.1999 (m/s)
   Sound speed (equilibrium) 1065.437 (m/s)
   Gamma frozen) 1.2519 (m/s)
   Gamma (equilibrium) 1.1593 (m/s)
Reflected Shock
   Speed  811.4007 (m/s)
   Pressure 6528749.7919 (Pa)
   Temperature 3784.4415 (K)
```

C Cantilever Beams

A simple cantilever beam is used in the ES1 testing to make force measurements. The geometry is shown in Fig. 26 and the engineering drawings used in fabrication are shown in Fig. 29. We can use simple beam theory (Chap. 5 Ugural and Fenster, 1987) to find the relationship between load, deflection, and strain. For a load P that is aligned with the $+y$ axis through the centroid of the beam, the resulting deformation is pure bending and the strains are given by

$$\epsilon_x = -\frac{M_z y}{E I_z} \tag{107}$$

$$\epsilon_y = -\nu \epsilon_x \tag{108}$$

$$\epsilon_z = -\nu \epsilon_x \tag{109}$$

where the bending moment at the strain gage location x_{sg} is

$$M_z = -\int y \sigma_x \, dA \tag{110}$$

and this can be computed from the moment of force balance and the applied loads as

$$= \int_{x_{sg}}^{x_{beam}} F(x) \, dx \; . \tag{111}$$

For a concentrated applied load at location x_P, the bending moment at the strain gage location is

$$= P(x_p - x_{sg}) \; . \tag{112}$$

The moment of inertia about the neutral axis (which is taken to coincide with the z axis) of the beam cross section is

$$I_z = \int y^2 dA \tag{113}$$

which for the rectangular beam shown in Fig. 26 is

$$I_z = \frac{1}{12} b h^3 \; . \tag{114}$$

Evaluating these expressions at the upper surface of the beam $y = h/2$, the strain is related to the load by

$$\epsilon_{sg} = \frac{6P(x_{sg} - x_p)}{bh^2 E} \tag{115}$$

$$\tag{116}$$

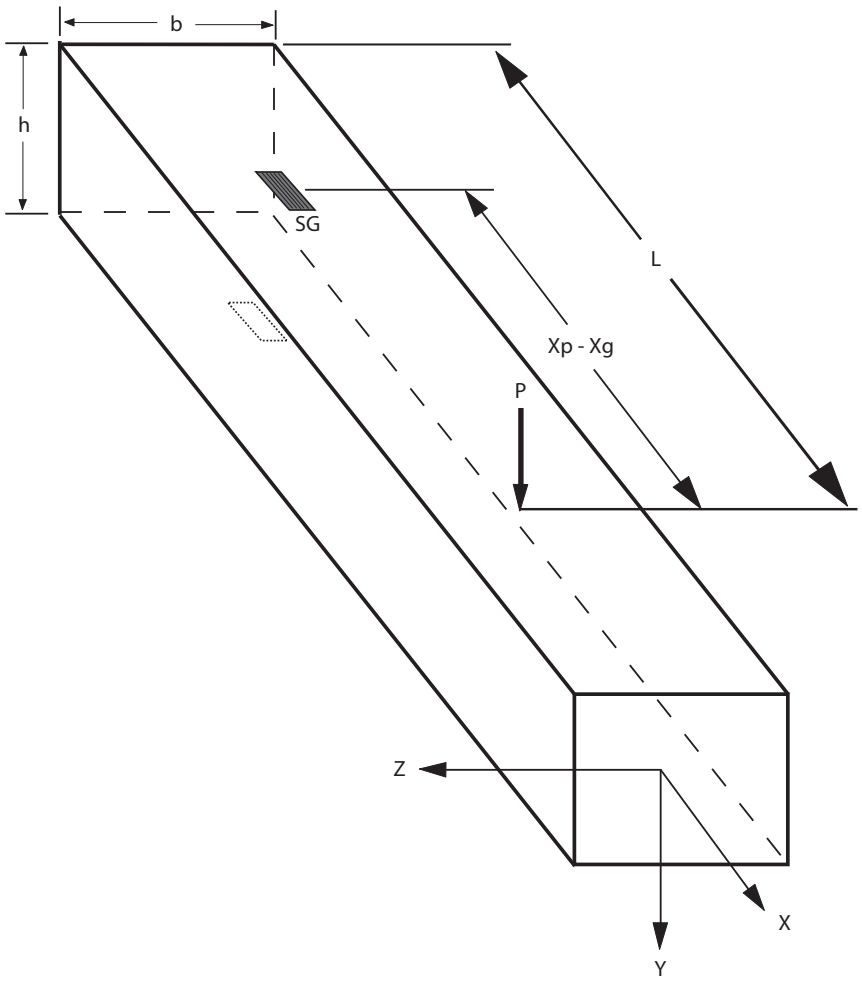

Figure 26: Cantilever beam used for force measurement. Strain gage (SG) and mirror image are located at a distance x_g and the load force P is applied at distance x_p.

In order to compensate for axial loads and thermal effects, a pair of gages located diametrically opposite and wired in a half-bridge configuration is usually recommended Bray et al. (1990), Perry (2008). The second gage location is shown in dashed outline on Fig. 26. The gages are located in adjacent arms of the Wheatstone bridge as shown in Fig. 27. The

voltage output of the bridge will be

$$V_{out} = V_{exc}\frac{K}{2}\epsilon \tag{117}$$

where the gage factor is K and the excitation voltage is V_{exc}. Note that the output is twice a large as the usual quarter-bridge output. This is due to the location of strain gages SG1 and SG2 in adjacent legs of the bridge and assuming that one gage in always in tension and the other in compression with equal absolute strain magnitude in each gage. This requires that the pair of gages be carefully mounted at equal distances from the load and the neutral axis and also aligned with the x axis of the beam. If the bridge output voltage is multiplied

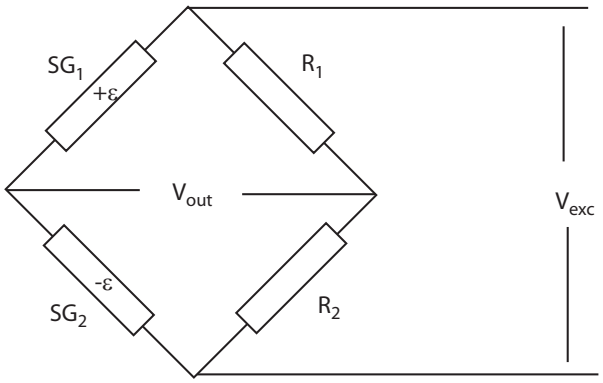

Figure 27: Half-bridge circuit used with a pair of strain gages mounted to measure bending as shown in Fig. 26.

by a signal conditioner with gain G, then the voltage V_{meas} that is recorded by the data acquisition is related to the bending strain ϵ by

$$\epsilon = \frac{2}{KGV_{exc}}V_{meas} \ , \tag{118}$$

Using a nominal gage factor of 2.105 and a gain of 1000, the strain (in μstrain units) is

$$\epsilon = 95.01V_{meas} \ . \tag{119}$$

For a static load of magnitude P, the force is related to the longitudinal strain at location x_{sg} by

$$P = \frac{Ebh^2}{6(x_p - x_{sg})}\epsilon \ . \tag{120}$$

For the beams used in the ES1 experiments, the material was A36 steel with a nominal modulus of 210 GPa and the distance $x_p - x_{sg} = 3.5$ in (88.9 mm). The beam dimensions are $b = 1$ in (25.4 mm) and $h = 1.25$ in (31.75 mm) for deflections in the y direction. Using these values, the computed relation between force and strain on the beam in the vertical direction ($b = 1.00$ in, $h = 1.25$ in) is

$$P = 10.07\epsilon \ , \tag{121}$$

where P is in N and ϵ is in μstrain. In the horizontal direction, $b = 1.25$ in and $h = 1.00$ in, so that

$$P = 8.056\epsilon \ . \tag{122}$$

The cantilevers were calibrated by hanging test masses from a eyebolt connected to a hanger clamped to the cantilever at the location of the nominal load application 4.5 in from the root of the beam. The comparison between measured and predicted values of strain are shown in Fig. 28. Using a least-squares fit of the data, the proportionality constants were determined to be 10.004 N/μstrain in the 1.25 in direction and 8.078 N/μstrain in the 1.0 in direction. The linearity of the force-strain relation ($R^2 = 0.9999989$) and the agreement between the measured and computed values is within 0.3%, confirming the validity of the simple beam theory for interpreting the data.

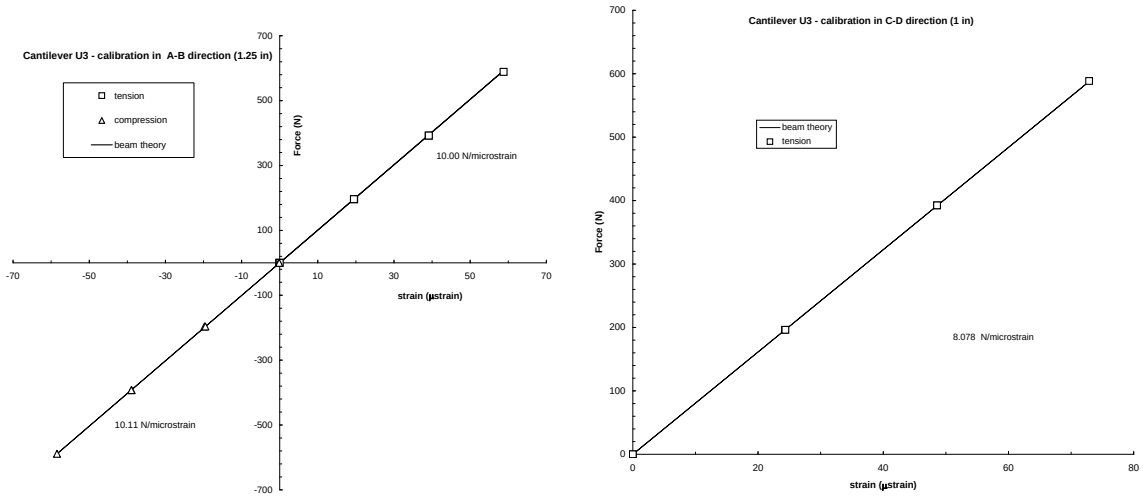

Figure 28: Calibration of cantilever beams and comparison with simple beam theory for force-strain relationship.

The beam vertical deflection can be computed as a function of the magnitude of the

applied load. This can be used to compute the effective stiffness or force constant of the beam. If we ignore the contribution of shear to the deflection, the static deflection Y of the point where the load is applied is

$$Y = \frac{Px_p^3}{3EI} \tag{123}$$

where x_p is the distance from the point of load application to the root of the beam. For the beams used in ES1, the point of load application is 4.5 in (114.3 mm) from the root of the beam and the total beam length was 7 in (177.8 mm), we have

$$Y = 3.508 \times 10^{-8} P \ , \tag{124}$$

or 35.08 μm per kN of applied load. This can also be written as a spring constant

$$P = k_y Y \ , \tag{125}$$

where the spring constant is

$$k_y = \frac{3EI}{x_p^3} \ , \tag{126}$$

$$= 2.851 \times 10^7 \quad \text{N/m} \ . \tag{127}$$

In the horizontal direction, the stiffness is lower since $h = 1.$ in for this direction of deflection, so that $k_x = 1.825 \times 10^7$ N/m.

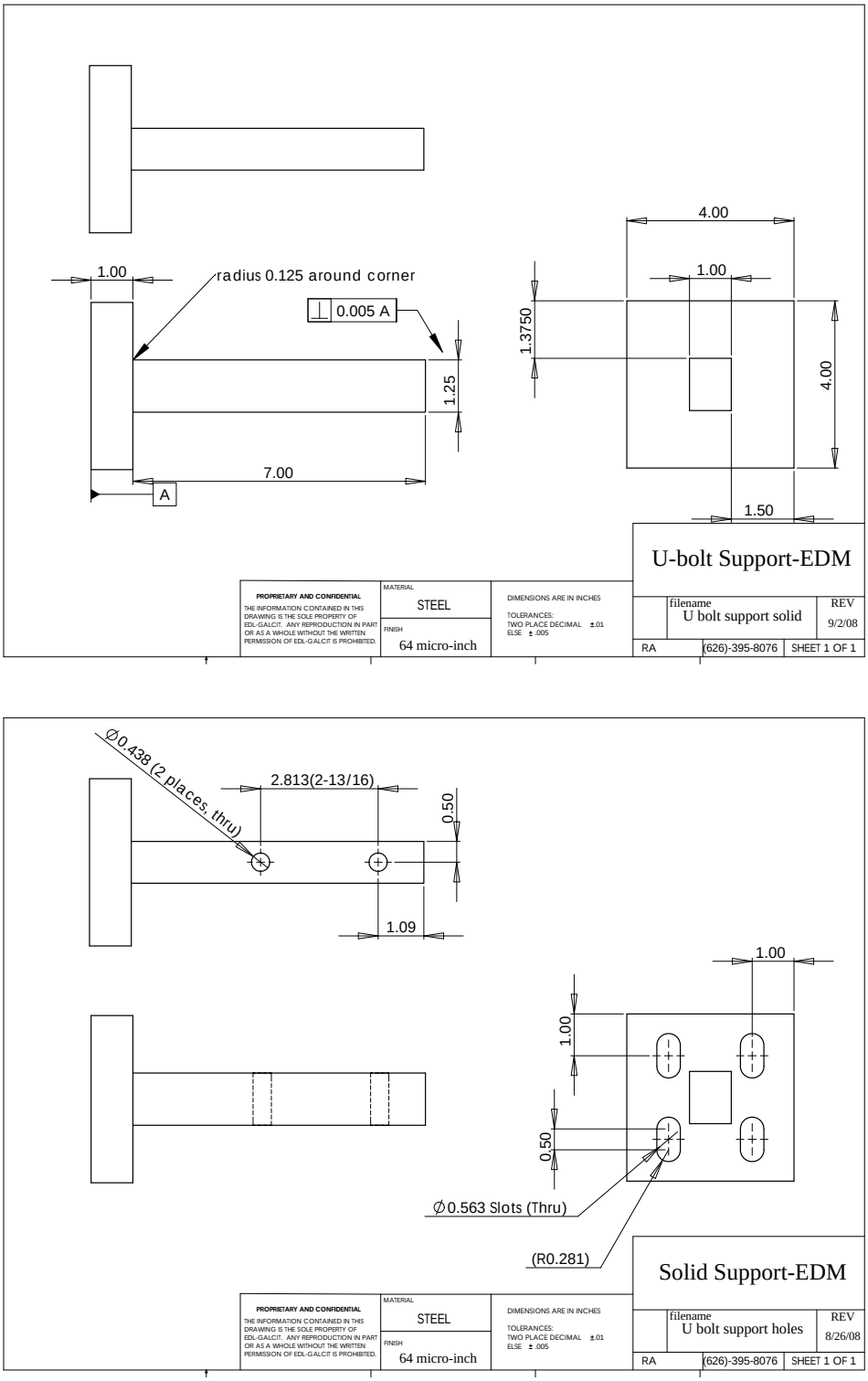

Figure 29: Fabrication drawings used to construct cantilever beams from a single billet of steel.

C.1 Dynamic response

The dynamic response of the cantilever beams was tested by striking the beam (oriented with the 1.25 in axis parallel to the hammer motion) with an instrumented impact hammer (PCB Model 086D05) at the nominal load application point P shown in Fig. 26. The results of recording the impact force and beam bending strain response in a representative test are shown in Fig. 30. The applied force is a single impulse of 2 ms duration with a peak load of about 1.2 kN. The strain signal is measured at the location SG shown in Fig. 26. The strain appears to respond essentially quasi-statically to the initial force and following the end of the load, the beam responds by oscillating with a much lower amplitude at a frequency near the fundamental bending mode of ~800 Hz. The measured force is compared with the force obtained by interpreting strain quasi-statically using (120) and the value (121) appropriate to this orientation. As shown, the quasi-static interpretation is adequate for an estimate of the peak value for this simple loading history but does not capture the true peak value or correct load history at times later than 4 ms.

A more accurate reconstruction of the force history can be obtained by using the experimental data to find a frequency response function (McConnell, 1995) or using a FEM model (Doyle, 2004) to invert the strain measurements. A simpler alternative which we will use in interpreting the strain data obtained in the ES1 tests (see Section 5.2) is to model the response as a single-degree-of-freedom (SDOF) system and use parameter identification methods to determine the effective stiffness K and mass M. The SDOF model presumes that the system can be represented as a forced harmonic oscillator and the deflection Y is determined by the undamped equation of motion (92). Assuming the deflections are proportional to the measured beam bending strains (103), we have the approximate equation of motion

$$M\alpha\frac{d^2\epsilon}{dt^2} + K\alpha\epsilon = F(t) \tag{128}$$

where α is given in (104). Using the Savitzky-Golay method (MathWorks) with a third-polynomial fit to obtain the second-derivative of the strain, an unconstrained minimization was used to find the values of M and K that gave a minimum L-2 norm difference between the measured and computed forces. Four tests were examined and each test gave slightly different sets of parameters (M, K). For the test shown in Fig. 30, the optimum values were M = 1.74 kg and $K\alpha$ = 10.7 N/μstrain. These values are quite reasonable in comparison to the physical parameters that can be computed or measured. The mass of the cantilever bar (see Fig. 29) is 1.15 kg and the mass of the base is 0.524 kg. The static force constant $K\alpha = k_y$ obtained from either beam theory or measurements is given above at 10.07 N/μstrain.

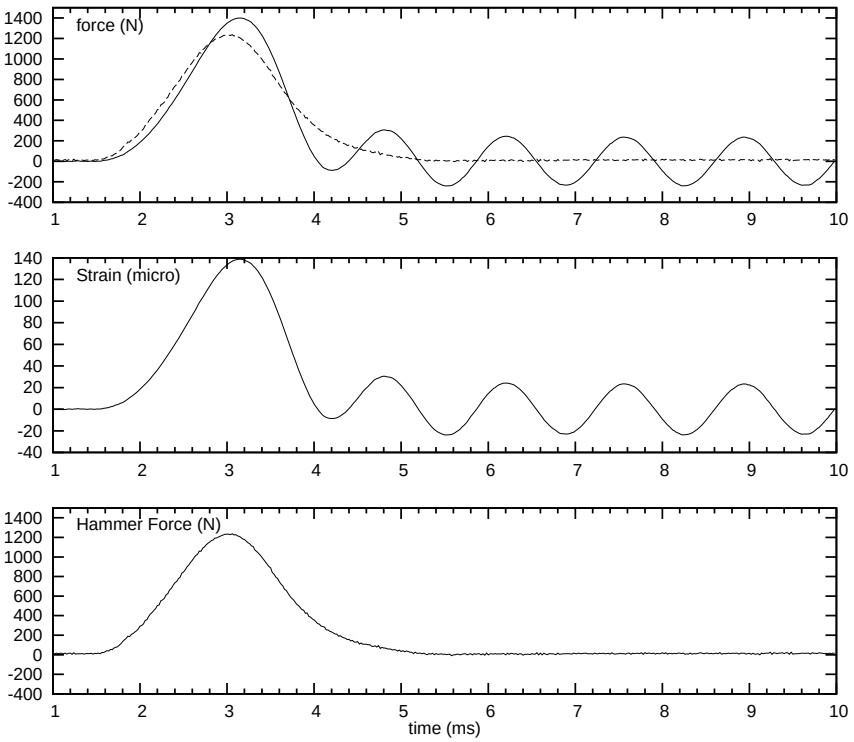

Figure 30: Hammer strike test on free cantilever beam. Bottom: force measured by impact hammer. Middle: Strain measured on struck surface 1 in from base of beam. Top: Comparison of quasi-static force predicted from strain with actual force from impact hammer.

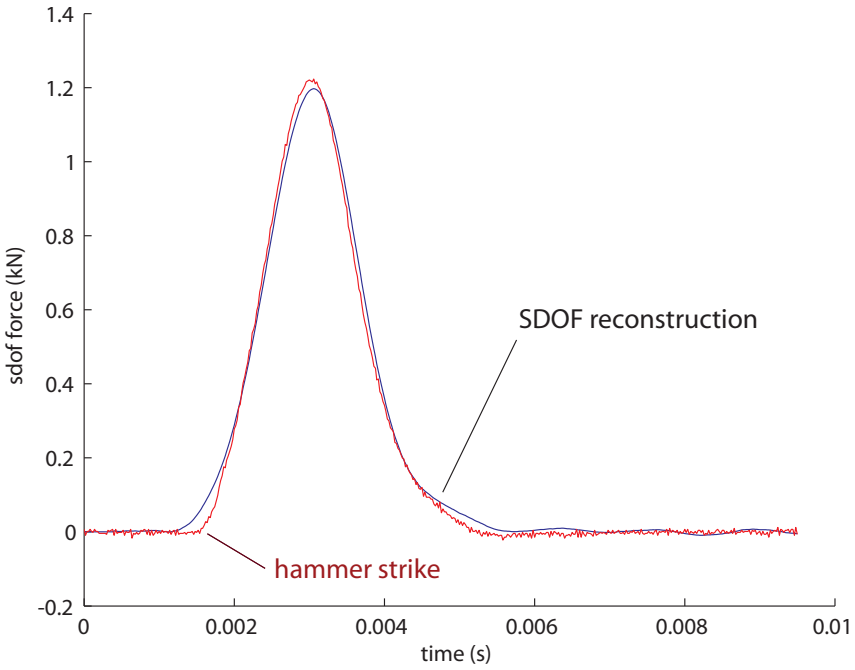

Figure 31: Comparison of SDOF model reconstructed force with measured hammer strike force for test of the free cantilever beam shown in Fig. 30.

The SDOF model appears to capture most of the essential dynamics of the system for the relatively slow loading function imposed in the hammer strike. For higher frequency (shorter duration forces) motion, flexural waves on the beam must be considered (see Chap. 3 of Doyle, 1997a). When the cantilever is attached to the piping system, the dynamics of the coupled cantilever-piping system are substantially different than the free cantilever. As discussed in Section 5.2, very different parameters (particularly the effective mass) will have to be used even if the SDOF approximation is retained. However, the results shown in Fig. 31 indicate that if the SDOF model is valid, then reasonable results for force can be obtained once the correct parameters are identified.

D Piping System Low Frequency Modes

A finite element model of the ES1 piping system (SolidWorks COSMOS 2008 SP3 version) was used to analyze the possible vibration modes with various conditions on the end of the pipe and selected results are given below.

Five models of ES1 were created and analyzed. All models restrained the upper-left end to be fixed (see Fig. 3), have the pipe itself made of 304 Stainless Steel of inside diameter 2.067 in. and outer diameter 2.375 in., and take the horizontal portion to be 3.6 m long followed by a bend of 8-in radius and a vertical portion of 1.7 m.

The difference between the models is in how the lower-right end is constrained. In Model 1, this end is fixed. In Model 2, it is allowed to slide in the out-of-plane, or x-, direction (i.e., into and away from the wall in the actual set-up) and restrained in all other directions. Model 3 allows movement in the up direction (z-direction) but uses a spring of spring constant $k = 2.72 \cdot 10^7$ N/m to constrain this movement; movement in the side-to-side directions (x and y) is not allowed. Model 4 uses springs to constrain both the up (z) direction with $k_u = 2.72 \cdot 10^7$ N/m and in the side-to-side (y) direction (parallel to the wall) with $k_s = 1.74 \cdot 10^7$ N/m, movement into and away from the wall (x) is not allowed. Model 5 supports the lower-right end with a cantilever beam fixed to the wall as occurs in the actual experiment. A summary of the first ten vibrational frequencies is given in Table 4. The first part of the table is for In-Plane frequencies—these are the frequencies we're expecting to excite—and the second part of the table is for the Out-Of-Plane frequencies. Note that Model 5 has some coupling between the in-plane and out-of-plane directions that increases with increasing mode frequency. The results of Model 1 can be compared with the ANSYS computations given in Table 1. Except for the modes at 85 and 89 Hz, there is a reasonable match between the frequencies for the two methods of computation.

The models deemed most important are Model 1, due to its simplicity, and Model 5, due to its accuracy. Perspective views of representative deformations indicating the mode shapes for these two models are presented in the subsequent figures.

Figure 32: Geometry of Model 5 of ES1.

Table 4: Vibration frequencies for five models of ES1.

In-Plane Frequencies					
Mode	Model 1	Model 2	Model 3	Model 4	Model 5
1	21 Hz	20 Hz	20 Hz	20 Hz	20 Hz
2	58 Hz	56 Hz	46 Hz	46 Hz	49 Hz
3	85 Hz	82 Hz	64 Hz	64 Hz	66 Hz
4	128 Hz	123 Hz	114 Hz	114 Hz	112 Hz
5	200 Hz		142 Hz		114 Hz*
6					129 Hz

Out-Of-Plane Frequencies					
Mode	Model 1	Model 2	Model 3	Model 4	Model 5
1	10 Hz	3 Hz	5 Hz	5 Hz	8 Hz
2	25 Hz	11 Hz	22 Hz	21 Hz	23 Hz
3	61 Hz	25 Hz	43 Hz	43 Hz	53 Hz
4	89 Hz	59 Hz	66 Hz	66 Hz	72 Hz
5	132 Hz	87 Hz	116 Hz	111 Hz	
6		128 Hz		135 Hz	

**This mode had strong components in both the in-plane and out-of-plane directions.*

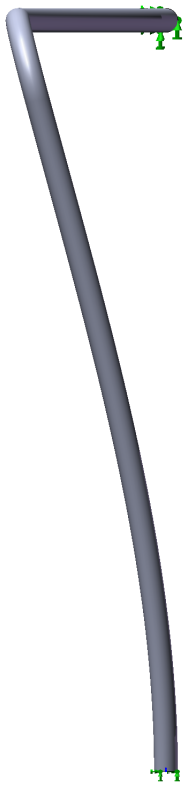

Figure 33: Model 1, Mode 1: $f = 10$ Hz

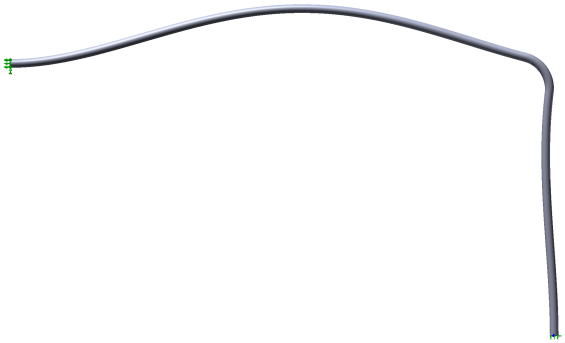

Figure 34: Model 1, Mode 2: $f = 21$ Hz

Figure 35: Model 1, Mode 3: $f = 25$ Hz

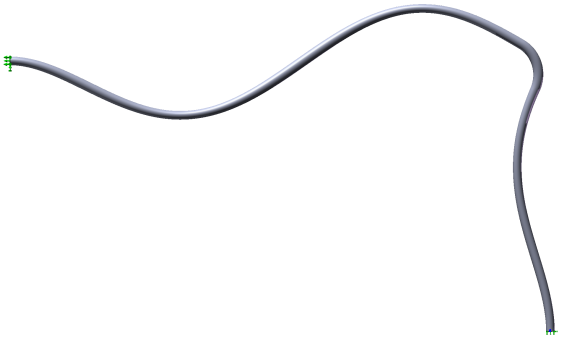

Figure 36: Model 1, Mode 4: $f = 58$ Hz

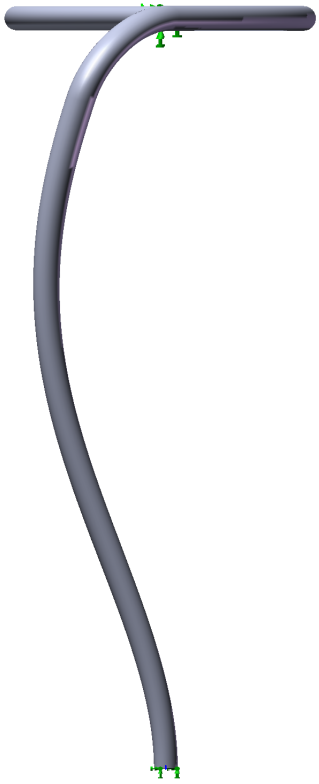

Figure 37: Model 1, Mode 5: $f = 61$ Hz

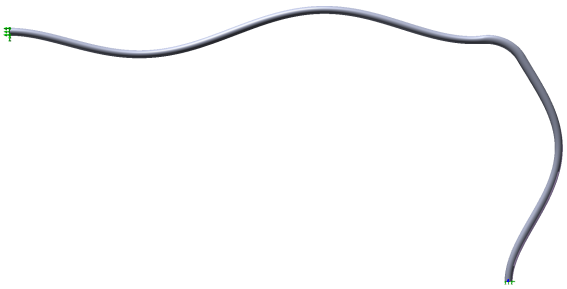

Figure 38: Model 1, Mode 6: $f = 85$ Hz

Figure 39: Model 1, Mode 7: $f = 89$ Hz

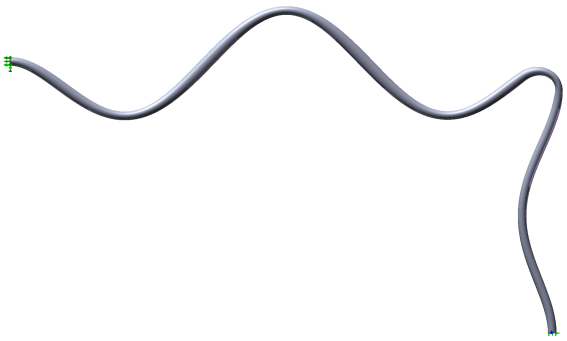

Figure 40: Model 1, Mode 8: $f = 128$ Hz

Figure 41: Model 1, Mode 9: $f = 132$ Hz

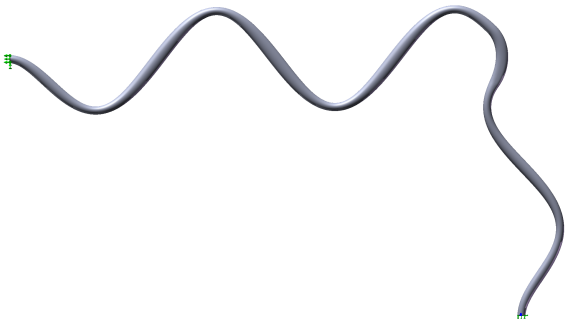

Figure 42: Model 1, Mode 10: $f = 200$ Hz

Figure 43: Model 5, Mode 1: $f = 8$ Hz

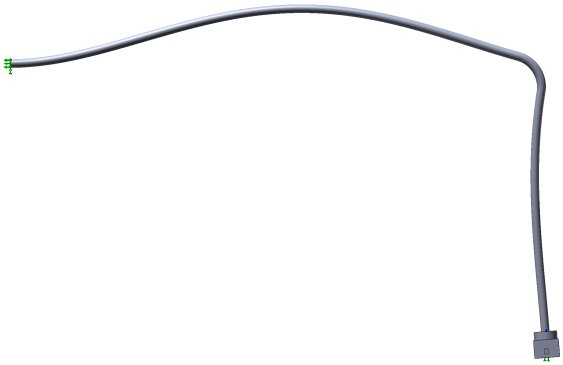

Figure 44: Model 5, Mode 2: $f = 20$ Hz

Figure 45: Model 5, Mode 3: $f = 23$ Hz

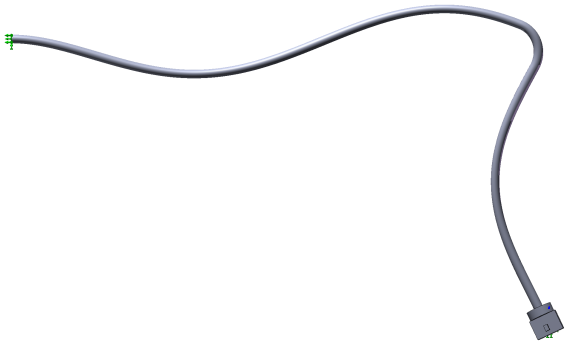

Figure 46: Model 5, Mode 4: $f = 49$ Hz

Figure 47: Model 5, Mode 5: $f = 53$ Hz

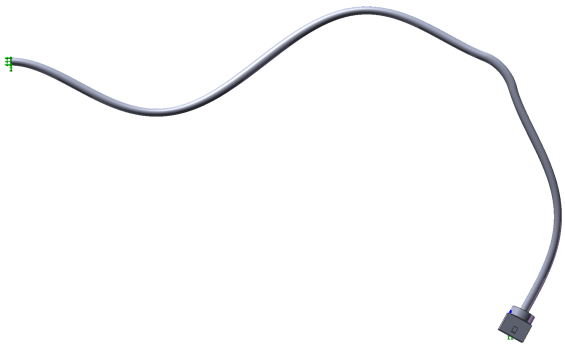

Figure 48: Model 5, Mode 6: $f = 66$ Hz

Figure 49: Model 5, Mode 7: $f = 72$ Hz

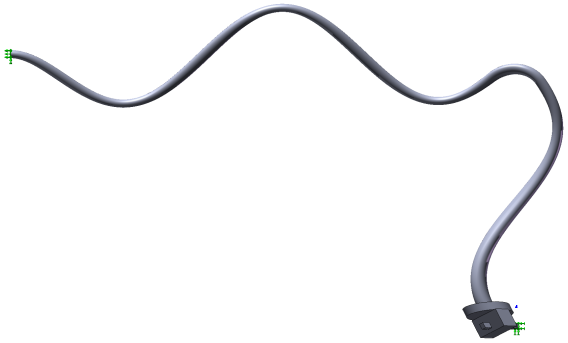

Figure 50: Model 5, Mode 8: $f = 112$ Hz

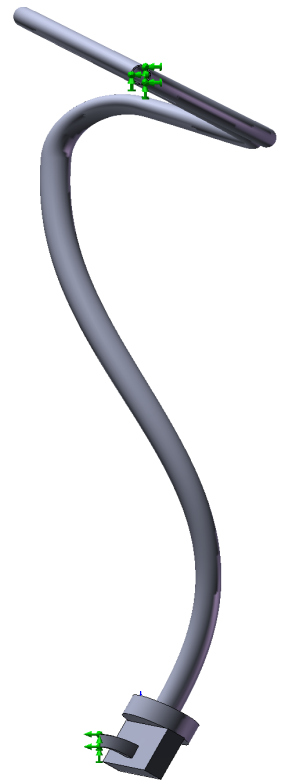

Figure 51: Model 5, Mode 9: $f = 119$ Hz

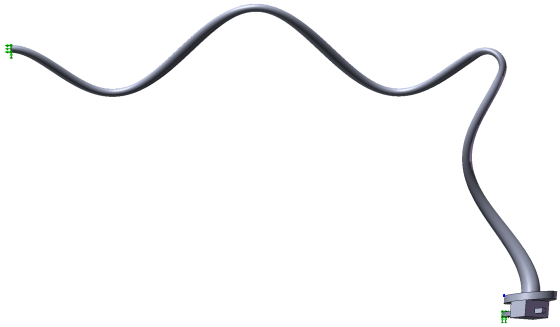

Figure 52: Model 5, Mode 10: $f = 129$ Hz

Figure 53: Model 5, Mode 11: $f = 155$ Hz

Figure 54: Model 5, Mode 12: $f = 175$ Hz

Figure 55: Model 5, Mode 13: $f = 201$ Hz

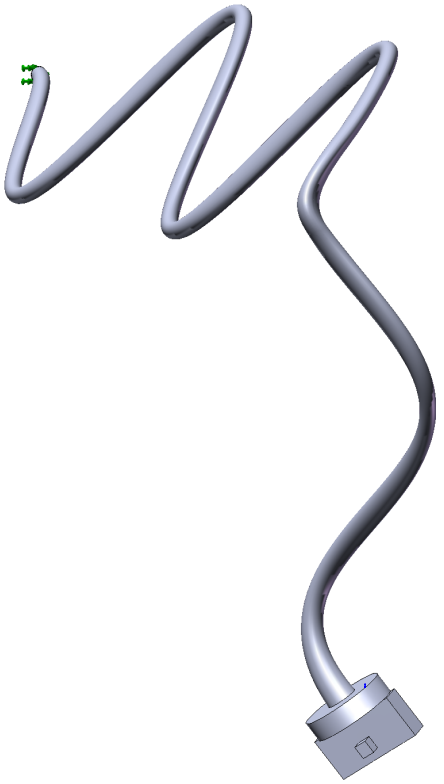

Figure 56: Model 5, Mode 14: $f = 213$ Hz

Figure 57: Model 5, Mode 15: $f = 257$ Hz

Figure 58: Model 5, Mode 16: $f = 283$ Hz

Figure 59: Model 5, Mode 17: $f = 303$ Hz

Figure 60: Model 5, Mode 18: $f = 314$ Hz

Figure 61: Model 5, Mode 19: $f = 348$ Hz

Figure 62: Model 5, Mode 20: $f = 374$ Hz

E Stiffness of the Fixed Anchors

The fixed anchors used to connect the piping to the plates and wall are constructed of 1-in thick steel (A36) plate with a robust design intended to resist deformation due to detonation initiation or reflection; see Figures 63-67.

The actual stiffness of the anchors was investigated using static simulations to determine the deflection under prescribed loads that simulate axial loads transferred from the piping system to the anchors. The contours of deflection are shown for two cases in Fig. 68 and representative values are given in Table 5.

Case A. Load is applied to central 6 inch annulus centered about 3.125 in hole of anchor front plate with 3-sides held fixed.

Case B. Load is applied to central 6 inch annulus centered about 3.125 hole of anchor front plate with back surface portion (the surface region that meets normally with the side and bottom plates) held fixed.

Table 5: Deflections of anchor plates for two static loading cases.

case	load (N)	location	deflection (μm)	stiffness (N/m)
A	4454.54	free edge	5	8.91×10^8
A	4454.54	center	2.5	1.78×10^9
B	4454.54	free edge	3.27	1.36×10^9
B	4454.54	center	2.5	2.72×10^9

The conclusion is that the anchor plate is between 30 and 100 times stiffer (in terms of equivalent spring constant or stiffness factor k) than the cantilever beams (considering the value of k_y given in Appendix C) used for the U-bolt supports and force link.

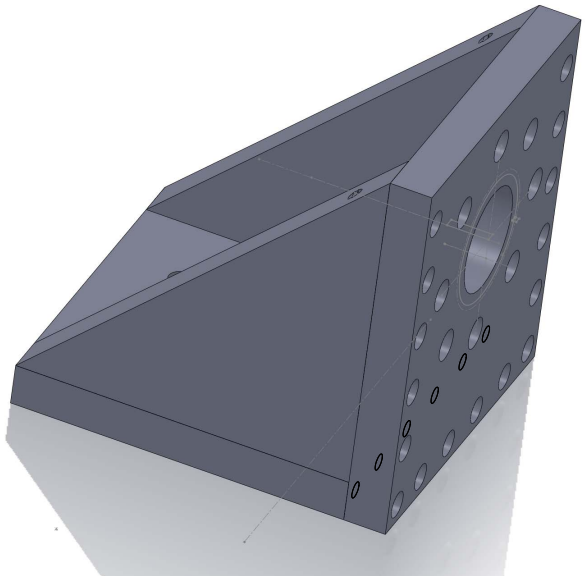

Figure 63: Perspective view of fixed anchor for ES1.

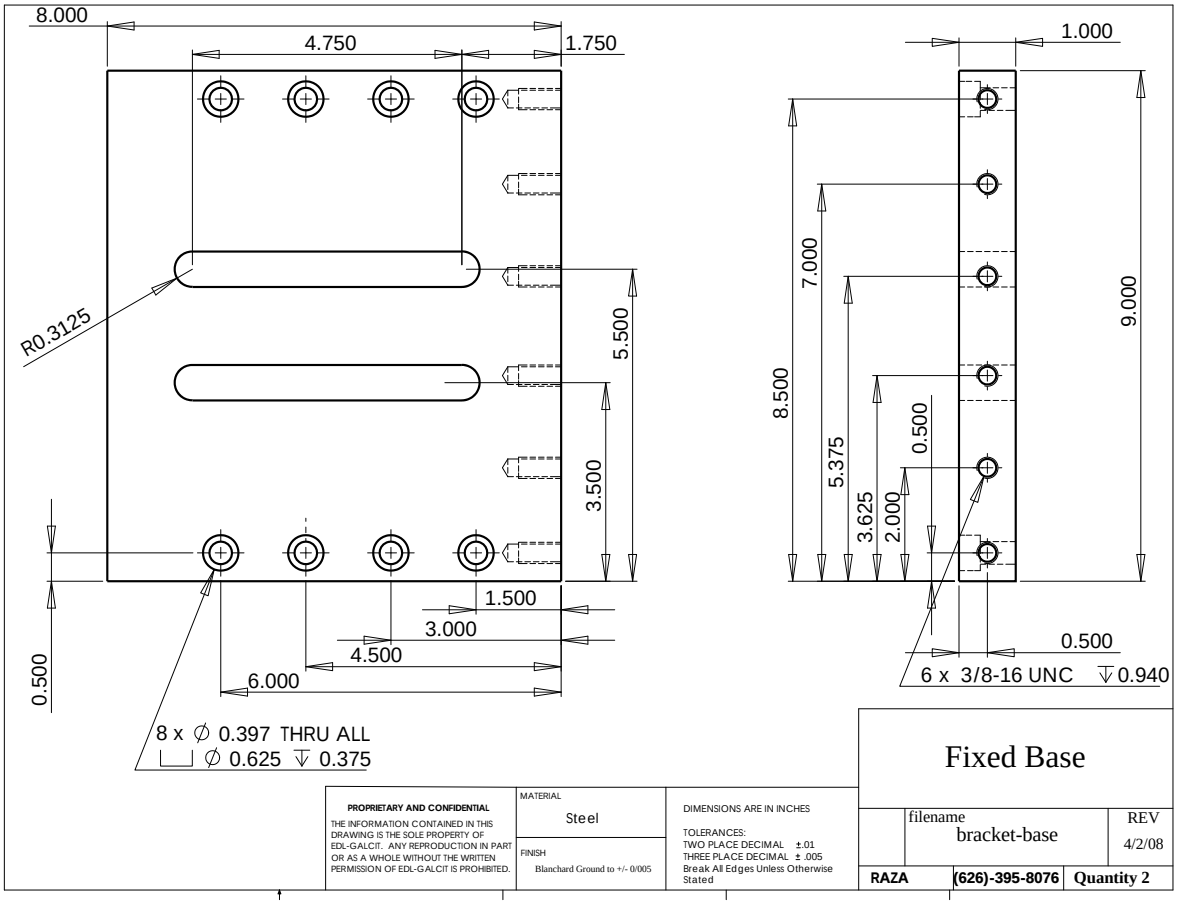

Figure 64: Engineering drawing of base of anchor for ES1.

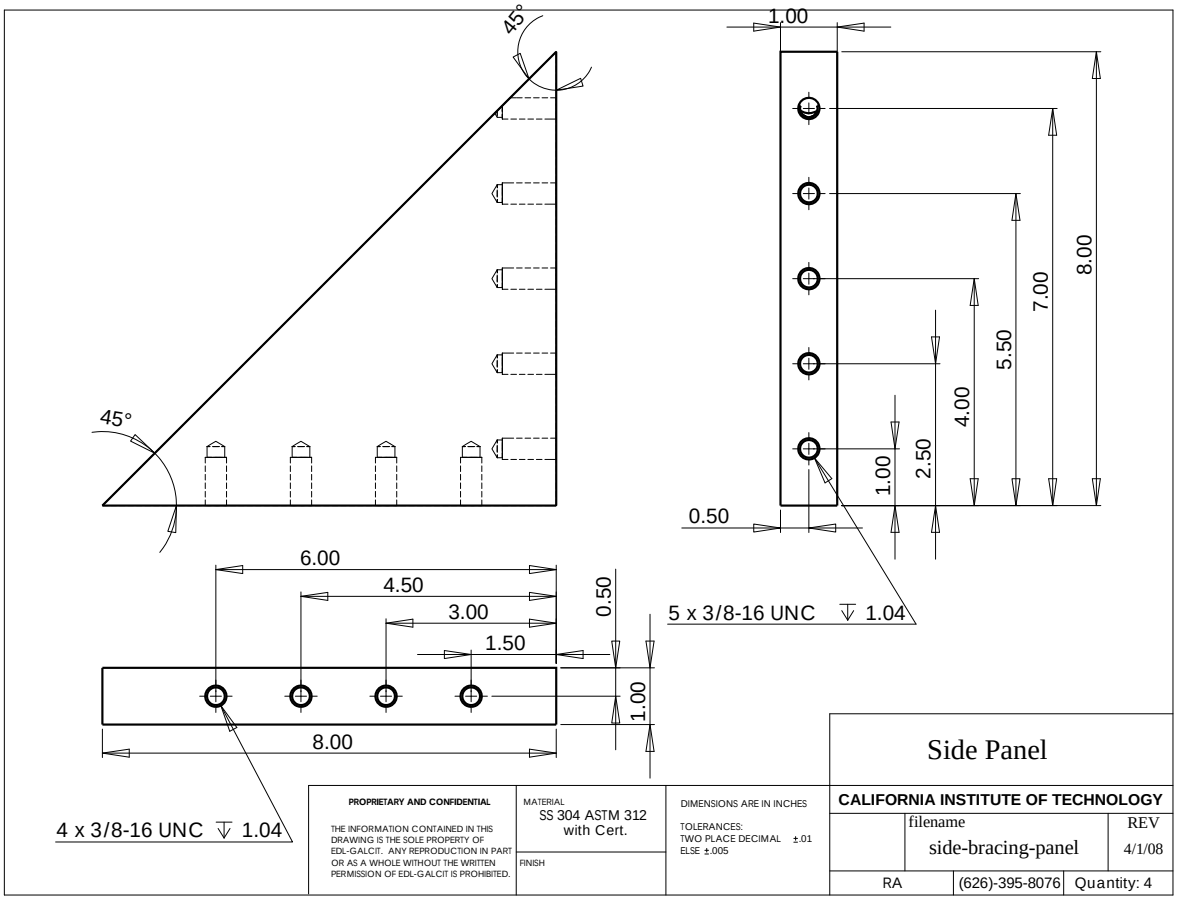

Figure 65: Engineering drawing of side brace of anchor for ES1.

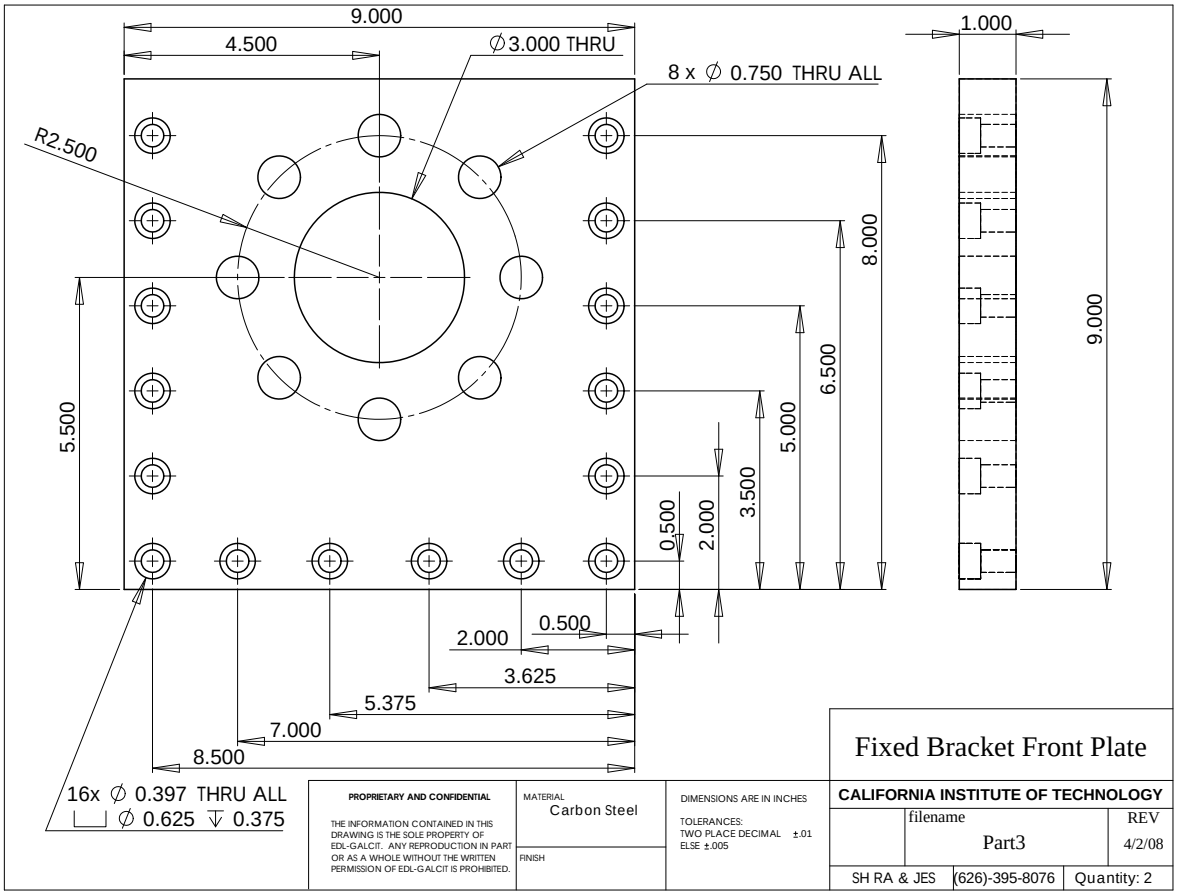

Figure 66: Engineering drawing of front of anchor for ES1.

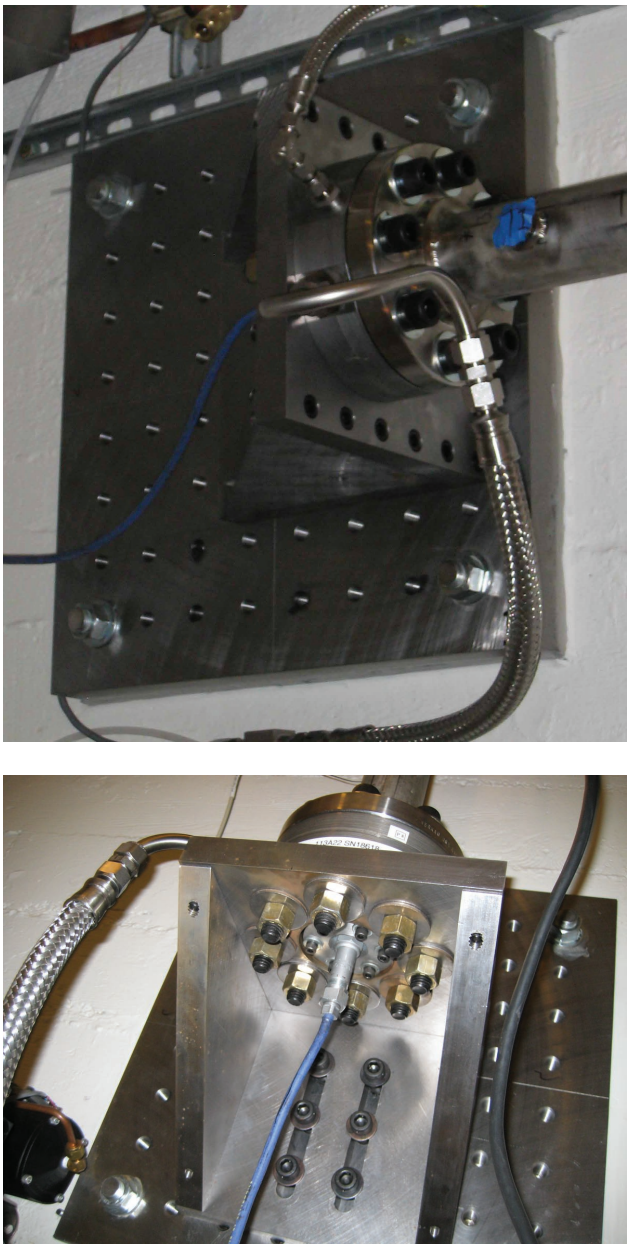

Figure 67: Photographs of front and back of fixed anchor attached to ES1 and wall mounting plates.

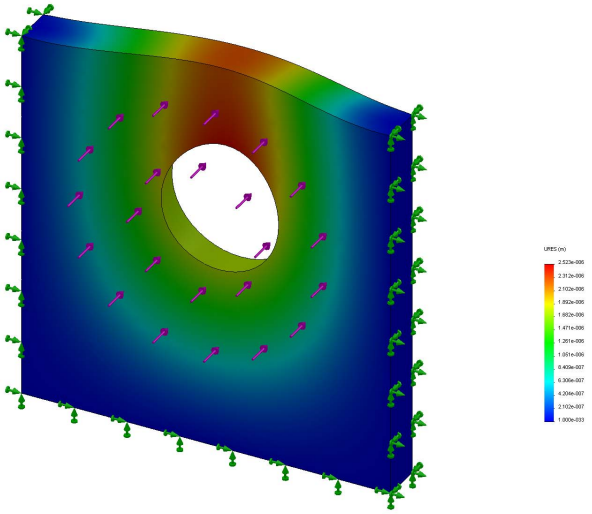

A.

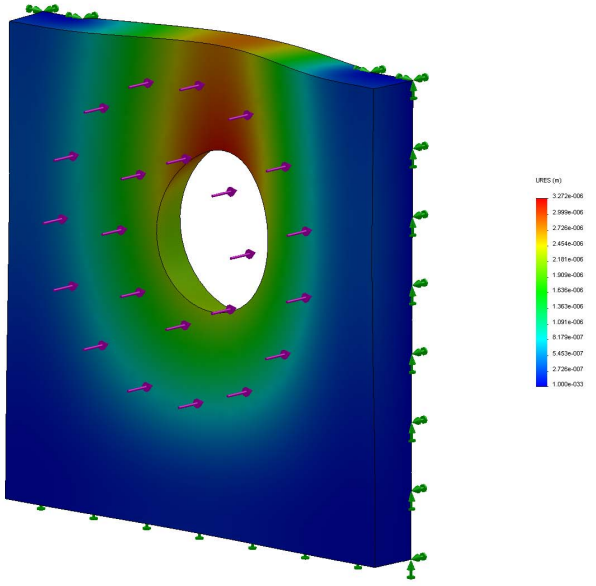

B.

Figure 68: Deflection distribution for two loading conditions for the front plate of the anchors.